



ALMA MATER STUDIORUM  
UNIVERSITÀ DI BOLOGNA

ARCHIVIO ISTITUZIONALE  
DELLA RICERCA

## Alma Mater Studiorum Università di Bologna Archivio istituzionale della ricerca

What steers the “folding to faulting” transition in carbonate-dominated seismic fold-and-thrust belts? New insights from the Eastern Southern Alps (Northern Italy)

This is the final peer-reviewed author’s accepted manuscript (postprint) of the following publication:

*Published Version:*

Zuccari, C., Viola, G., Curzi, M., Aldega, L., Vignaroli, G. (2022). What steers the “folding to faulting” transition in carbonate-dominated seismic fold-and-thrust belts? New insights from the Eastern Southern Alps (Northern Italy). *JOURNAL OF STRUCTURAL GEOLOGY*, 157, 1-20 [10.1016/j.jsg.2022.104560].

*Availability:*

This version is available at: <https://hdl.handle.net/11585/882440> since: 2023-01-11

*Published:*

DOI: <http://doi.org/10.1016/j.jsg.2022.104560>

*Terms of use:*

Some rights reserved. The terms and conditions for the reuse of this version of the manuscript are specified in the publishing policy. For all terms of use and more information see the publisher's website.

This item was downloaded from IRIS Università di Bologna (<https://cris.unibo.it/>).  
When citing, please refer to the published version.

(Article begins on next page)

This is the final peer-reviewed accepted manuscript of:

Zuccari C.; Viola G.; Curzi M.; Aldega L.; Vignaroli G.: What steers the “folding to faulting” transition in carbonate-dominated seismic fold-and-thrust belts? New insights from the Eastern Southern Alps (Northern Italy)

JOURNAL OF STRUCTURAL GEOLOGY Vol. 157 ISSN 0191-8141

DOI: 10.1016/j.jsg.2022.104560

The final published version is available online at:

<https://dx.doi.org/10.1016/j.jsg.2022.104560>

Rights / License:

The terms and conditions for the reuse of this version of the manuscript are specified in the publishing policy. For all terms of use and more information see the publisher's website.

*This item was downloaded from IRIS Università di Bologna (<https://cris.unibo.it/>)*

***When citing, please refer to the published version.***

1           **What steers the “folding to faulting” transition in**  
2           **carbonate-dominated seismic fold-and-thrust belts?**

3           **New insights from the Eastern Southern Alps**

4                                   **(Northern Italy)**

5                           Zuccari C.<sup>1</sup>(\*), Viola G.<sup>1</sup>, Curzi M.<sup>1</sup>, Aldega L.<sup>2</sup> and Vignaroli G.<sup>1</sup>

6  
7           <sup>1</sup> Alma Mater Studiorum, University of Bologna, Department of Biological, Geological and Environmental  
8           Sciences - BiGeA, Bologna, Italy.

9           <sup>2</sup> Sapienza, University of Rome, Department of Earth Sciences, Rome, Italy.

10  
11  
12  
13  
14  
15           **\*Corresponding author:**

16           **Costantino Zuccari**

17           Dipartimento di Scienze Biologiche, Geologiche e Ambientali  
18           Alma Mater Studiorum – Università degli Studi di Bologna  
19           Via Zamboni, 67 – 40126 Bologna (Italy)

20           [costantino.zuccari2@unibo.it](mailto:costantino.zuccari2@unibo.it)

21           [+393398768039](tel:+393398768039)

22

23

24

25

26

27

28

29

30

31

32

33

34

35

36

37

38

39

40

41

42

43

44

45 **Abstract**

46         Several parameters steer the modes of shortening of carbonate-dominated fold-and-thrust belts  
47 from incipient- (layer parallel shortening, buckle folds) to evolved deformation stages (verging folds,  
48 discrete thrusts). In this study, we address the spatial and temporal evolution of compressive  
49 structures within carbonate-dominated fold-and-thrust belts by documenting the geometry,  
50 kinematics and structural architecture of the San Donato-Costa Thrust Zone, a splay of the regional  
51 Belluno Thrust of the seismically active Eastern Southern Alps (Northern Italy). Deformation is there  
52 accommodated by a variety of features ranging from open and upright to tight and verging folds cut  
53 by later thrusts. An integrated structural analysis indicates inherited primary features to have  
54 effectively steered the deformation style of the thrust and its immediate hanging wall and footwall.  
55 We propose an evolving deformation scenario initially governed by the inherited lithological features  
56 and localised pressure-solution, then by the geometry of folds accommodating progressive shortening  
57 and, finally, by thrusting. The folding-faulting transition occurs when forelimbs dip  $\sim 80^\circ$  and the  
58 ratio between the dip angle of fore- and back limbs is  $\sim 3.3$ . These geometric boundary conditions  
59 control the mechanical behaviour of carbonate multilayer successions during orogenic shortening in  
60 fold-and-thrust belts, assisting the partitioning between seismic and aseismic deformation.

61

62 **Keywords:** Eastern Southern Alps; Folding-faulting transition; Carbonate multilayers; Mechanical  
63 stratigraphy; Seismic behaviour; Seismic vs. aseismic.

64

65

66

67

68

## 69 **1. Introduction**

70 Deformation in carbonate rocks in any given geodynamic setting is steered and modulated by  
71 a broad spectrum of boundary conditions. Among others, i) rock type and mechanical stratigraphy,  
72 ii) pressure and temperature, iii) stress field orientation, iv) presence and composition of fluids, v)  
73 presence and spatial distribution of inherited sedimentary and structural anisotropies, such as bedding,  
74 foliation planes and inherited faults, seem to play a key role in governing the deformation style both  
75 in compressive and in extensional settings (Stewart and Hancock, 1991; Bigi et al., 2003; Billi et al.,  
76 2003; Billi, 2010; Labaume et al., 2004; Collettini et al., 2009; Cilona et al., 2012; Fagereng et al.,  
77 2014; Michie et al., 2014; Bussolotto et al., 2015; Ikari et al., 2015; Tavani et al., 2015; Delle Piane  
78 et al., 2017).

79 In carbonate-dominated fold-and-thrust belts folding and thrusting can coexist to accommodate  
80 deformation at all scales. Folding is commonly associated with aseismic creep whereas thrusting  
81 occurs mainly by cyclic seismic rupturing (e.g., Erickson, 1996; Ruh et al., 2012; Swanson et al.,  
82 2012; Tesei et al., 2013; Tavani et al., 2015; Bigi et al., 2018; Curzi et al., 2020). Also, the  
83 compositional heterogeneity of carbonates, which is due to inherently different marl/limestone ratios  
84 and to the primary porosity, plays a significant role in the localisation of deformation during both  
85 diffuse folding (Ramsay and Graham, 1970; Fischer and Jackson, 1990; Micarelli et al., 2006; Tondi  
86 et al., 2006; Dautriat et al., 2011; Cilona et al., 2012, 2014; Lena et al., 2015; Nabavi and Fossen,  
87 2021) and discrete (seismic) thrusting (Tavani et al., 2008; Smith et al., 2011; Collettini et al., 2013;  
88 Bullock et al., 2014; Michie, 2015; Giorgetti et al., 2016). Understanding the evolution of folding and  
89 faulting and their mutual relationships in space and through time is, thus, key to the unravelling and  
90 constraining of progressive deformation histories and seismogenesis of carbonate-dominated fold-  
91 and-thrust belts (Ramsay, 1974; Tavarnelli, 1997; Simpson, 2009; Hudleston and Treagus, 2010;  
92 Kilian et al., 2011; Tavani et al., 2015; Tavarnelli et al., 2021).

93 It is widely documented that the transition from upright and symmetric buckle folds to more  
94 mature, tight to asymmetric folds occurs in response to the progressive accommodation of distributed  
95 deformation ([Hudleston et al., 1996](#); [Butler et al., 2020](#); [Humair et al., 2020](#)). Faulting, on the other  
96 hand, is the result of deformation localisation associated with the progressive increase of shortening,  
97 as documented by numerical models and field studies (e.g., [Lacombe et al., 2007](#); [Simpson, 2009](#);  
98 [Humair et al., 2020](#); [Kilian et al., 2021](#)). In particular, faulting in a progressively developing fold-  
99 and-thrust belt occurs when folds reach their lock-up stage such that no further shortening can be  
100 accommodated by their continued tightening and amplification (e.g., [Ramsay, 1974](#); [Fischer et al.,](#)  
101 [1992](#); [Simpson, 2009](#); [Butler et al., 2019](#)). Two crucial issues regarding the folding-faulting transition  
102 are, however, still poorly addressed and, thus, understood:

- 103 (i) is there a given quantifiable deformation threshold beyond which folding gives way to  
104 faulting?
- 105 (ii) (ii) which parameters steer this transition and the switch of deformation mechanisms in  
106 carbonate multilayer successions? (e.g., [Marques, 2008](#); [Simpson, 2009](#); [Hudleston and](#)  
107 [Treagus, 2010](#); [Humair et al., 2020](#)).

108 Addressing these issues is important not only to the understanding of the geometrical, kinematic,  
109 mechanical and rheological behaviour of carbonate-dominated fold-and-thrust belts, but also to the  
110 characterisation of first-order mechanisms of deformation and strain localisation at all scales and of  
111 seismogenesis at large, the study of which commonly relies upon only indirect constraints (e.g.,  
112 seismic imaging,  $V_p/V_s$  and tomographic analysis, geodetic velocity analysis; e.g., [Chiarabba et al.,](#)  
113 [2005](#); [Carminati et al., 2007](#); [Anselmi et al., 2011](#); [Serpelloni et al., 2016](#); [Anderlini et al., 2020](#)).

114 To help bridge this knowledge gap, here we document the geometry, kinematics and structural  
115 architecture of the San Donato-Costa Thrust Zone, a splay of the regional Belluno Thrust ([Zuccari et](#)  
116 [al., 2021](#)), which deforms a multilayer carbonate succession of the seismically active central Eastern  
117 Southern Alps of Northern Italy ( $M_w > 6.0$  earthquakes; [Galadini et al., 2005](#); [Carminati et al., 2007](#);

118 [Anselmi et al., 2011](#); [Serpelloni et al., 2016](#); [Anderlini et al., 2020](#)). Based on the systematic analysis  
119 of well-preserved structures that are representative of both the local early contractional phase (i.e.,  
120 the first discrete increments of shortening of the Eastern Southern Alps) by distributed folding and of  
121 later thrusts, we document and constrain the transition from folding to thrusting during progressive  
122 deformation. We show that the folding-faulting transition is governed by the progressive growth and  
123 tightening of asymmetric folds leading first to the progressive increase of the dip angle of their  
124 forelimbs and, finally, to discrete rupturing and thrusting. For the first time, we propose a numerical  
125 threshold for this transition based on the geometrical characteristics of the folded multilayer sequence,  
126 and we discuss this in the framework of the overall mechanical/seismic behaviour of fold-and-thrust  
127 belts.

128

## 129 **2. Geological setting**

### 130 **2.1 The Eastern Southern Alps**

131 The Eastern Southern Alps (hereafter ESA) are a fold-and-thrust-belt of the south-verging retro-  
132 belt of the European Alps ([Fig. 1a and b](#)), which developed during the Cretaceous-to-Neogene  
133 convergence between Europe and Adria (e.g., [Doglioni and Carminati, 2008](#)). The ESA have been  
134 shaped by several tectonic events including:

- 135 i) E-W crustal extension during the Permo-Triassic rifting leading to the development of  
136 N-S trending and orogen-scale faults and significant calcalkaline volcanism ([Winterer  
137 and Bosellini, 1981](#); [Doglioni, 1987](#); [Bosellini et al., 2003](#); [Schaltegger and Brack,  
138 2007](#));
- 139 ii) Middle Triassic differential subsidence and local uplift, climaxing into a magmatic  
140 event during Late Ladinian times (e.g., [Castellarin et al., 1988](#); [Bosellini et al., 2003](#);  
141 [Lustrino et al., 2019](#); [De Min et al., 2020](#));



- 142           iii)     Rifting starting in the Late Triassic and climaxing during the Early Jurassic (e.g.,  
143                    [Bosellini et al., 2003](#); [Handy et al., 2010](#));
- 144           iv)     Cenozoic-Alpine compression, which began during the Cenozoic Europe-Adria  
145                    convergence and continental collision and which is still active ([Doglioni, 1987](#);  
146                    [Castellarin and Cantelli, 2000](#); [Carminati et al., 2004](#); [Schmid et al., 2004](#); [Castellarin](#)  
147                    [et al., 2006](#); [D'Ambrogi and Doglioni, 2008](#)).

148            These tectonic phases are well recorded within the local ESA sedimentary succession that rests  
149            upon igneous and metamorphic basement rocks of Palaeozoic age ([Fig. 1b and c](#)). This > 3 km thick  
150            sedimentary cover is made up of Permian - Lower Triassic siliciclastic units, overlain by Middle  
151            Triassic - Lower Jurassic shallow-water carbonates ([Fig. 1c](#); [Bosellini et al., 1981](#); [Trevisani, 1991](#);  
152            [Masetti et al., 1998](#)). The succession ends at the top with Lower Jurassic-Neogene cherty pelagites  
153            and hemipelagites capped by Palaeocene-to-Miocene terrigenous and bioclastic formations ([Fig. 1b,](#)  
154            [c](#); [D'Alberto et al., 1995](#); [Stefani et al., 2007](#)).

155            The still ongoing Alpine compression that ensued during the Cenozoic has been and is being  
156            accommodated by south-verging thrusts and associated folds ([Doglioni, 1992](#); [Castellarin and](#)  
157            [Cantelli, 2000](#)) and ~ 30 km of cumulative shortening is estimated across the ESA (e.g., [Doglioni,](#)  
158            [1992](#)). From the late Tortonian to the early-Middle Pleistocene, shortening was accompanied by  
159            repeated fluctuations of the principal stress directions (from NNW-SSE to NW-SE; [Caputo et al.,](#)  
160            [2010](#)). Most crustal shortening, however, had already occurred during the late Oligocene (e.g.,  
161            [Doglioni, 1992](#); [Castellarin and Cantelli, 2000](#); [Castellarin et al., 2006](#)) and localised along six main  
162            thrusts that formed in sequence from north to south: Valsugana, Belluno, Moline, Tezze, Bassano-  
163            Maniago and the Montello thrusts ([Doglioni, 1990](#); [Doglioni and Carminati, 2008](#); [Fig. 1b and c](#)).  
164            The Belluno Thrust (hereafter BT) is the focus of our study. It exhibits a ramp-flat geometry and  
165            forms a ~ 20 km long WSW-ENE-striking and ~ 30° N-dipping thrust ([Fig. 1b-d](#)) that accommodated  
166            a total shortening of ~ 6-8 km ([Selli, 1998](#); [D'Ambrogi and Doglioni, 2008](#)). Multiple tectonic and

167 seismogenic reactivations characterised the mechanical behaviour of the BT during significant strain  
168 localisation in carbonate-dominated rocks (Vignaroli et al., 2020). In the hanging wall of the BT, a  
169 regional-scale anticline deforming Jurassic-Lower Cretaceous units is characterised by a sub-vertical  
170 to overturned forelimb and a  $\sim 20^\circ$  N-dipping back limb subparallel to the BT slip plane (Figs. 1b, c,  
171 and 2). In the footwall there occurs the San Donato-Costa Thrust Zone (hereafter SCTZ), a second-  
172 order splay of the BT, which cuts across an Upper Jurassic-lower Eocene sedimentary succession  
173 (Zuccari et al., 2021; Fig. 1d).

174 From a seismotectonic perspective, the ESA are characterised by still active seismic  
175 contractional deformation, as documented by recent and historical seismicity (Fig. 1a and d;  
176 Serpelloni et al., 2016; Carminati et al., 2007; Anderlini et al., 2020). The available seismological  
177 dataset shows that seismicity mostly localises within the ESA southernmost edge and its Triassic-to-  
178 Paleogene carbonate succession along the transition to the Venetian Plain (Bassano–Maniago Thrust  
179 and Montello Thrust, Fig. 1), with events up to  $M_w \geq 6$ , as documented by a historical record spanning  
180 > 1000 years (Galadini et al., 2005; Cheloni et al., 2014; Serpelloni et al., 2016).

181

### 182 3. Methods

183 Our work focuses on the folded and faulted carbonate succession in the footwall of the BT,  
184 along and across the SCTZ. We integrated detailed field structural mapping and mesoscale structural  
185 analysis with XRD diffraction of 17 samples collected along the studied San Donato-Costa section  
186 (Fig. 3a and b). The exposed sedimentary succession was mapped at the 1:2,500 and 1:5,000 scale  
187 (Zuccari et al., 2021) and further characterised from a paleontological and lithological perspective to  
188 constrain its multilayer character with alternating “pure” and cherty limestone, marly-limestone and  
189 marl (Fig. 3c).

190 A detailed field structural analysis was carried out along N-S oriented transects (parallel to the  
191 sense of tectonic transport) to assess the deformation and structural style as a function of the distance  
192 from the SCTZ. Systematic mesoscopic structural observations aimed to define the first-order  
193 structural framework of the study area and the geometric relationships between folds and faults in the  
194 hanging wall, footwall, and the thrust zone itself. This quantitative geometrical and structural  
195 characterisation relies on the following parameters:

- 196 i)  $\alpha$ : bedding dip angle in fold back limb;
- 197 ii)  $\beta$ : bedding dip angle in fold forelimb;
- 198 iii)  $\delta$ : dip angle of thrust in fold back limb.

199 The characterisation of fold (a)symmetry is based on the length of back- and forelimbs, whereby  
200 asymmetric folds are defined by a long back limb and a short forelimb, followed by another long back  
201 limb (Twiss and Moores, 1992). We implement this approach with the concept of “fold envelope  
202 surface”, defined as “*the surface tangent to the individual hinges along fold layers*”, Fossen, 2016;  
203 Fig. S1). Considering a low dip angle envelope surface, an increasing length difference between back-  
204 and forelimb is also accompanied by the increase of the  $\beta/\alpha$  ratio (Fig. S1). It follows that the  $\beta/\alpha$   
205 ratio can be taken as a reliable indicator of fold (a)symmetry (Fig. S1).

206 X-ray diffraction was performed to define mineralogical and compositional heterogeneities  
207 within the multilayer succession and allow for the assessment of the mechanical implications thereof.  
208 Ten samples were collected from limestone beds and seven from calcareous marl layers (Fig. 3a,  
209 Tables S1 and S2). We refer the readers to the Supplementary Material for detailed information on  
210 the methodology and instrumentation.

211

212

213

## 214 4. Results

### 215 4.1 Structural framework of the San Donato - Costa Thrust Zone

216 The SCTZ cuts across an up to 650 m thick carbonate multilayer succession (Figs. 1d, 2 and  
217 3). From bottom to top, this succession includes: i) the Rosso Ammonitico Veronese (Bajocian *p.p.* -  
218 upper Tithonian *p.p.*), which consists of massive to well-bedded nodular red and grey limestone and  
219 marly limestone; ii) the Maiolica Fm. (upper Tithonian *p.p.* - lower Aptian), an up to 300 m thick  
220 succession of cherty limestone with alternating 5-10 cm thick marly beds toward the top (Fig. 3b and  
221 c); iii) the Scaglia Variegata Alpina Fm. (lower Aptian - lower Turonian *p.p.*), formed by a ca. 30 m  
222 thick marly and clay rich lower member (Fig. 3c) and by a ~ 50 m thick more calcareous upper  
223 member (Fig. 3b and c); iv) the Scaglia Rossa Fm. (lower Turonian *p.p.* - lower Eocene *p.p.*), formed  
224 by a ca. 150 m thick well bedded sequence of marl and calcareous marl (Fig. 3c). The succession is  
225 capped by ~ 110 m of marl and shale with rare calcareous intercalations (Marna della Vena d'Oro  
226 Fm., upper Palaeocene - lower Eocene *p.p.*, Fig. 3c).

227 The SCTZ is a 2 km long, E-W-striking and SSE verging thrust defined by a main single slip  
228 plane in its eastern sector, which passes into several anastomosed fault-splays in the west (Figs. 2, 3a  
229 and b). The estimated stratigraphic throw along the SCTZ is up to ~ 60 m in the east, whereas it  
230 progressively increases up to several hundred meters toward the west (Fig. 3a and b). The hanging  
231 wall of the SCTZ is folded by a km-scale anticline (Figs. 2 and 3a) with a steep-to-subvertical S-  
232 dipping forelimb made of the Maiolica Fm. (Fig. 3b). The immediate footwall of the SCTZ is formed  
233 by an overturned syncline cored by the Scaglia Rossa Fm. (Figs. 2 and 3a-b). Mesoscopic parasitic  
234 fold trains occur along the ~ 20° NNW-dipping back limb of the hanging wall anticline and along the  
235 ~ 20° NNW-dipping forelimb of the footwall syncline (Fig. 3a and b). These parasitic folds are locally  
236 cut across by top-to-the SE mesoscopic thrusts, that accommodate centimetric to metric offsets, and  
237 are spatially arranged in mesoscale duplexes in the Scaglia Rossa Fm. along the syncline forelimb.

238 In the following, we illustrate the main structures of the SCTZ by taking a virtual journey from  
239 the hanging wall in the north to the footwall in the south (Fig. 3).

240

#### 241 4.1.1 Hanging wall of the San Donato - Costa Thrust Zone

242 The northernmost portion of the considered hanging wall section (i.e., hundreds of metres far  
243 away from the SCTZ; Figs. 2 and 3) contains evidence of bedding-perpendicular pressure solution  
244 within the Maiolica Fm. (Figs. 4a and 5). Pressure solution planes systematically abut against  
245 bedding. This is evident within both tabular (Fig. 5a and b) and not folded domains as well as in  
246 symmetric buckle folds (Fig. 5c), where pressure solution planes are invariably perpendicular to  
247 bedding, irrespective of their position within the fold (Fig. 5d-f). This observation suggests that  
248 pressure solution planes formed prior to folding (Fig. 5c-f). Pressure-solution planes are at a constant  
249 spacing of ~ 10 cm within the same bed (Fig. 5a), although spacing tends to increase with bed  
250 thickness (Fig. 5c). Traces of insoluble material are locally preserved and define the pressure solution  
251 planes (Fig. 5b). The latter are generally tabular and rather smooth. Minor N-dipping thrust planes  
252 dipping at ~ 35° ( $\delta$ ) locally exploit bed-bed interfaces (Fig. 5b) and cut across the bed-perpendicular  
253 pressure solution planes (Fig. 5b). Such thrust planes are systematically found along the tabular  
254 portions of the succession where they are decorated by slickenlines and slickenfibres, which  
255 invariably indicate a top-to-the SE sense of shear (Fig. 5b).

256 Moving to the SCTZ, the number of folds in the hanging wall increases while their wavelength  
257 decreases (Figs. 2, 3a-b, 6a). There, Maiolica limestones deformed by open and upright folds (Fig.  
258 4d) lack evidence of pressure solution (Fig. 6b). Open folds have wavelengths in the 3-5 m range,  
259 amplitudes up to 2 m, and symmetric shapes with comparable dip angle for both limbs ( $\alpha$  and  $\beta$  =  
260 32°; Figs. 4b and 6b). Farther to the south and close to the SCTZ, folds wavelength and amplitude  
261 decrease to an average of ~ 90 cm and ~ 40 cm, respectively (Fig. 6c and d). Folds tend to become  
262 south-verging and more asymmetric, with back limbs dipping to the NW ( $\alpha$  = 35°) and forelimbs to

263 the SE ( $\beta = 50^\circ$ ; Figs. 4b and 6c). In place, folds are locally faulted by bed-parallel, top-to-the SE  
264 thrusts that dip toward the NW ( $\delta = 35^\circ - 40^\circ$ ) and accommodate centimetric to metric offsets along  
265 bed-bed interfaces (Fig. 6c). As one approaches the SCTZ (Fig. 3a and b, Fig. 6a), the fold wavelength  
266 decreases further, and folds tend to tighten even more as part of a clear strain gradient (Fig. 6d). Their  
267 wavelength and amplitude decrease and back limbs and forelimbs dip toward the NW ( $\alpha = 50^\circ - 65^\circ$ )  
268 and to the SE ( $\beta = 55^\circ - 70^\circ$ ), respectively (Figs. 4b and 6d).

269 While the deformation structures described above deform the calcareous Maiolica Fm. along  
270 the western termination of the SCTZ, in the eastern part of the hanging wall the Scaglia Rossa Fm. is  
271 exposed. The deformation style therein is significantly different as it is mostly distributed (Figs. 3a  
272 and 7). In particular, pervasive S-C fabrics mainly affect the steeply dipping or overturned fold limbs  
273 ( $\beta = 68^\circ - 75^\circ$ ). The steeply dipping fold limbs are commonly dissected by closely spaced C planes  
274 (Fig. 7a, c and d). Locally, deformation is also accommodated by foliated domains within the marly  
275 layers of the Scaglia Rossa Fm. (Fig. 7b), which develop along NW-dipping bed-bed interfaces. S-C  
276 fabrics mostly indicate a top-to-the SE sense of shear (Fig. 7a and b) that is consistent with the  
277 transport of the principal thrusts, and, only to a lesser extent, top-to-the NE shearing, probably related  
278 to a reactivation during localised back thrusting (Fig. 7c).

279

#### 280 4.1.2 The thrust zone

281 The actual SCTZ consists of tightly spaced (up to  $\sim 100$  m) thrust splays (Fig. 3a and b), which  
282 cut the overturned Maiolica Fm. and the marly beds of the Scaglia Variegata Alpina Fm. (Fig. 3b).  
283 The thrust zone is well exposed along a  $\sim 100$  m long road section that exposes the main thrust and a  
284 lower basal splay (Figs. 8 and 9). This domain contains asymmetric and faulted folds within the  
285 overturned Maiolica Fm. (Fig. 8b) that exhibit pronounced south-verging geometries (Fig. 9b-d), with  
286 ENE-WSW-trending fold axes (Fig. 4b) and axial planes dipping NNW at  $45^\circ - 50^\circ$  (Figs. 4d and 9).  
287 Folds exhibit thickened hinges associated with local marl migration from the limbs (Fig. 9e) during

288 progressive folding. The marly domains in the hinge zones represent centimetric interbeds and are  
289 foliated (Fig. 9e), with foliation planes converging toward the hinge. Thrust planes bear slickenlines  
290 and stepped calcite slickenfibres indicating a top-to-the SSW sense of shear (Fig. 4c). Discrete, N-  
291 dipping ( $\delta = 30^\circ - 40^\circ$ ) second order thrust planes are commonly observed in the back limbs of  
292 mesoscopic folds, where they mostly localise along thin marly interbeds (Fig. 9b) or along gently  
293 dipping ( $\alpha = 35^\circ - 40^\circ$ ) bed-bed interfaces. Thrust planes accommodate offsets up to a maximum of  
294 a few decimeters (Fig. 9c) and cut across the steeply dipping ( $\beta = 78 - 85^\circ$ ) to overturned forelimbs  
295 (Fig. 9b and d) at high angle. They are associated with laterally continuous layers and lenses of  
296 cataclasite, formed by heterometric calcareous and cherty clasts embedded within a fine-grained  
297 cataclastic matrix (Figs. 9c and S2). Clasts are angular and derive from both the hanging wall and  
298 footwall and exhibit evidence of rigid-body rotation (Figs. 9c and S2). Sub-horizontal calcite veins  
299 locally decorate the thrust planes that cut through the highly dipping bedding in the forelimbs at an  
300 angle close to  $90^\circ$  (Fig. 9c).

301         Within the upper and overturned portion of the Maiolica Fm. (~ 250 m from the main thrust,  
302 Figs. 3, 8 and 9a), folds remain asymmetric and strongly verging to the SSE, with back- and forelimbs  
303 dipping at  $25^\circ - 30^\circ$  ( $\alpha$ ) and at  $60^\circ - 70^\circ$  ( $\beta$ ), respectively and with axial planes dipping toward the  
304 NNW at  $\sim 60^\circ$  (Figs. 4d and 9f). Marly interbeds are up to 20 cm thick and pervasively foliated in  
305 response to flexural slip and layer parallel shearing during progressive folding. On the gently dipping  
306 back limbs, these marly beds are deformed by diffuse foliation fabrics indicating a top-to-SE sense  
307 of shear (Fig. 9f).

308

#### 309 **4.1.3 Footwall of the San Donato - Costa Thrust Zone**

310         The footwall of the SCTZ is characterised by an overturned syncline with the more calcareous  
311 portion of the Scaglia Variegata Alpina Fm. and the Scaglia Rossa Fm. in the core (Fig. 3 and b). This  
312 domain is characterised by m-scale duplex structures defined by N-dipping ( $\sim 35^\circ$ ) and top-to-the SE

313 floor and roof thrusts (Fig. 10b and c). The stratigraphic succession above and below the duplexes is  
314 tabular and undeformed (Fig. 10b and c). Roof thrusts (Fig. 10d and e) dip to the NW ( $\delta = 15^\circ - 35^\circ$ )  
315 and invariably cut across the steeply dipping forelimbs ( $\beta = 60^\circ$ ) with a cut-off angle of  $\sim 45^\circ$  (Fig.  
316 10e). Within the duplexes, centimetric to decimetric horses and asymmetric lithons made of cherty  
317 beds and calcareous portions of Scaglia Rossa Fm. are embedded within pervasively foliated marls  
318 (Fig. 10b).

319 Moving toward the south into the upright limb of the footwall syncline, folds become more  
320 verging and asymmetric, defined by S-dipping ( $\beta = 75^\circ - 85^\circ$ ) or even overturned ( $\beta = 45^\circ - 60^\circ$ ) N-  
321 dipping forelimbs, whereas back limbs invariably dip toward the N-NE ( $\alpha = 25^\circ - 35^\circ$ ; Fig. 10d). Axial  
322 planes dip NE at  $\sim 50^\circ$  and fold axes trend ENE-WSW (Fig. 4a and b). Folds are commonly dissected  
323 by multiple N-dipping thrust splays that dip ( $\delta$ ) at  $\sim 20^\circ - 30^\circ$  and cut the fold hinge or the steeply  
324 dipping/overturned forelimbs (Fig. 10d). Interbed thrust planes commonly occur in the back limbs  
325 and extend toward the foreland (e.g., toward the south) cutting across the steep overturned forelimbs  
326 ( $\beta = 67^\circ - 79^\circ$ ; Fig. 10d). Weakly foliated cataclastic domains occur where thrusts cut the overturned  
327 forelimbs and the siliceous beds, mainly within the footwall of the thrusts (Fig. 10d and e).  
328 Deformation is particularly significant in the immediate surroundings of the main thrust surfaces (Fig.  
329 10d and e), as shown by increased fracture densities and locally weakly foliated cataclastic domains  
330 (Fig. 10e). On the contrary, foliated domains develop mainly where the thrusts exploit (on the back  
331 limbs) or cut (on the forelimbs) weaker marly beds (Figs. 10d and e). Foliation in marly beds is  
332 decorated by slickenlines and calcite slickenfibres indicating a top-to-the SSW sense shear (Figs. 4c  
333 and 10e). Calcareous sigmoidal lithons are embedded within the foliated marly domains (Fig. 10f).  
334 Foliated domains are bounded to the top and bottom by siliceous and stronger beds, which represent  
335 the mechanically strongest portion of the succession (Fig. 10d). All the kinematic indicators  
336 (slickenlines, calcite slickenfibres, and oblique foliation) are concordant with a top-to-the SSW sense  
337 of shear (Fig. 4c).



## 338 **4.2 X-ray diffraction of representative rock types**

### 339 **4.2.1 Calcareous beds**

340 The results of the X-ray semiquantitative analyses are shown in [Tables S1](#). Despite differences  
341 of stratigraphic age and structural position with respect to the main thrust surface, the mineralogical  
342 assemblage of limestone within the SCTZ sedimentary succession is quite similar throughout the  
343 entire analysed succession.

344 The limestone samples of the Maiolica Fm. belong to both the hanging wall (samples CZ2042,  
345 CZ2043, CZ2044, CZ2045, [Fig. 3b](#)) and footwall of the SCTZ (sample CZ2046, [Fig. 3b](#)). Their  
346 whole-rock composition is characterised by calcite contents between 91 wt % and 98 wt %,   
347 subordinate quartz (from 1 wt % to 7 wt %) and traces of Na-plagioclase and phyllosilicate minerals  
348 (K-white micas) that never exceed 2 wt %. Occasionally, traces of dolomite and rutile occur (sample  
349 CZ2042). Compared to the others, sample CZ2044 contains more quartz (13 wt %) because of the  
350 high radiolarian content and lower calcite amounts (85 wt %) than the rest of the samples.

351 The calcareous beds from the Scaglia Variegata Alpina Fm. (samples CZ2047, CZ2048,  
352 CZ2049, [Fig. 3b](#)) in the footwall domain of the SCTZ are composed of calcite with contents ranging  
353 from 93 wt % and 95 wt % and quartz that amounts to 3 - 5 wt %. Na-plagioclase and phyllosilicate  
354 minerals (K-white micas) occur with percentages lower than 2 wt %.

355 The Scaglia Rossa Fm. at the core of the footwall domain ([Fig. 3b](#)), contain calcite with contents  
356 between 82 wt % and 92 wt % and quartz that reaches up to 15 wt %. Accessory phases are albite,  
357 phyllosilicates (K-white micas) and hematite ([Table S1](#)).

358

### 359 **4.2.2 Calcareous-marly beds**

360 Calcareous-marly samples exhibit a stronger compositional variability than the limestone  
361 ([Table S2](#)). Samples from the Maiolica Fm. belong to the hanging wall (CZ2042Ma, CZ2043Ma, [Fig.](#)

362 3b) and footwall domains (CZ2052Ma, Fig. 3b). Samples CZ2042Ma, CZ2043Ma, from the upper  
363 portion of the Maiolica Fm., are composed of calcite (from 32 wt % to 72 wt %), quartz (15 - 37 wt  
364 %), phyllosilicate (9 - 27 wt %) and minor amounts of K-feldspar (< 3 wt %) and albite (> 3 wt %, [Table 2](#)).  
365 Sample CZ2052Ma, from the medium portion of the Maiolica Fm., displays a mineral  
366 assemblage and weight percent similar to those observed in the limestone with a slightly higher  
367 content of phyllosilicate (K-white mica, chlorite and mixed layered minerals). The higher quartz  
368 amount (37 wt %, sample CZ2042Ma, [Table S2](#)) is probably due to a local increase of the radiolarian  
369 content within the marly-calcareous matrix of the Maiolica Fm.

370 Calcareous marls from the Scaglia Variegata Alpina Fm. were collected in the footwall of the  
371 STCZ. Sample CZ2047Ma close to the thrust surface contains calcite (79 wt %), quartz (11 wt %),  
372 phyllosilicate (8 wt %, K-white mica, chlorite and mixed layered minerals), albite (2 wt %) and traces  
373 of hematite. Sample CZ2049Ma ([Table S2](#)), 500 m far away from the principal thrust surface ([Fig. 3a and b](#))  
374 has the same mineral content of the limestone samples with calcite weight percent of 95%  
375 and minor amounts of phyllosilicate minerals (3 wt %, K-white mica, chlorite and mixed layered  
376 minerals) and quartz (2 wt %).

377 Calcareous marls from the Scaglia Rossa Fm. at the core of the footwall syncline of the SCTZ  
378 ([Fig. 3b](#)) contain calcite as the most abundant mineral (90 - 93 wt %) followed by quartz (3-4 wt %).  
379 Furthermore, such samples display higher contents of phyllosilicate minerals (K-white mica and  
380 chlorite) than their limestone counterpart that amounts to 3 – 6 wt % of the overall composition.

381

## 382 **5. Data analysis, interpretation, and parametrisation**

383 We use our field observations and X-ray analyses to constrain the parameters that we believe  
384 have played a role in governing deformation and strain localisation within the studied carbonate  
385 succession. These are i) the thickness- and ii) the spatial distribution of marly layers, iii) the rock type

386 and phyllosilicate content and, finally, iv) the geometry of folds and thrusts. Although fluids are  
387 known to play a primary role in modulating (or influencing) deformation processes during progressive  
388 deformation (e.g., [Sibson, 1994](#); [Beaudoin et al., 2014](#); [Curzi et al., 2020, 2021](#); [Marchesini et al.,](#)  
389 [2019](#)), only a few syn-tectonic mineralisations (calcite slickenfibres and veins) are locally observed  
390 in the study area. Hence, our analysis just considers the role played by the primary features (i.e.,  
391 lithology, bedding) of the involved multilayer succession and does not explicitly account for fluid  
392 presence, composition and potential overpressuring.

393

## 394 **5.1 Thickness of marly layers**

395 We define a parameter to express the influence of the thickness of marly layers ( $t_m$ ; [Fig. 11](#)) in  
396 1 m of stratigraphic section by referring to the following dimensionless ratio:

$$397 \frac{\sum t_m}{T} \%$$

398 where  $\sum t_m$  is the cumulative measured thickness of marly layers in a reference stratigraphic section  
399 and  $T$  is the total measured stratigraphic thickness of the reference section. This ratio is highly variable  
400 throughout the studied succession. The Scaglia Rossa Fm. reaches values up to 43 % ([Fig. 11a](#)) and  
401 even 80 % in its upper portion, while the Maiolica Fm. exhibits the lowest calculated value (3 % - 24  
402 %, [Fig. 11b](#)). The parameter is intrinsically scale independent such that it can be applied to all scales  
403 of observation. Based on it, we define two representative endmembers to account for the deformation  
404 style of the entire studied stratigraphic succession: i) Scaglia Rossa type, with  $\sum t_m/T = 45$  % ([Fig.](#)  
405 [11a](#)), and ii) Maiolica type, with  $\sum t_m/T = 10$  % ([Fig. 11b](#)).

406

407

408

## 409 5.2 Spatial distribution of marly layers

410 The spatial distribution of marly layers within a measured multilayer succession (Fig. 11a and  
411 b) can be described by the ratio:

$$412 \frac{N_m}{T} \text{ (m}^{-1}\text{)}$$

413 where  $N_m$  represents the cumulative number of marly layers within the measured succession, and  $T$   
414 describes the reference stratigraphic thickness (1 m). The spatial distribution of marly layers also  
415 accounts for the thickness variation between marly ( $t_1$ ) and calcareous ( $t_2$ ) beds (Fig. 11a and b).

416 Within the analysed succession, the spatial distribution of the layers is generally regular, and their  
417 thickness seldomly exhibits significant changes. Marly beds are commonly thinner than calcareous  
418 beds. The Scaglia Rossa type endmember has  $N_m/T = 3 - 5 \text{ m}^{-1}$  ratio (Fig. 11a). The Maiolica type  
419 endmember, on the other hand, is described by  $N_m/T = 1 - 2 \text{ m}^{-1}$  (Fig. 11b), with only one or two marly  
420 layers within the measured succession. This chosen representative ratio for the endmembers is  $3 \text{ m}^{-1}$   
421 for the Scaglia Rossa type (Fig. 11a), and  $1 \text{ m}^{-1}$  for the Maiolica type (Fig. 11b).

422

## 423 5.3 Lithology and phyllosilicates content

424 The XRD data (Tables S1 and S2) of calcareous and calcareous-marly beds reveal that the  
425 main differences between the Maiolica and Scaglia Rossa types are exclusively due to the  
426 composition of the calcareous beds (Table S1). We consider the Maiolica type as composed of and  
427 best represented by calcareous beds where the phyllosilicate content is basically null (sample  
428 CZ2045, calcite = 98 wt %, phyllosilicates = 0 wt %; Table S1). The Scaglia Rossa type, instead, is  
429 represented by calcareous beds with a significantly lower calcite and higher phyllosilicate content  
430 with respect to the Maiolica type (sample CZ2051, calcite = 82 wt %, phyllosilicate = 2 wt %; Table  
431 S1).

432 The composition of the marly beds (Table S2), on the other hand, does not warrant the  
433 identification of the two principal endmembers. The composition of the calcareous-marly beds does  
434 not show a stark composition change within the succession, and we suggest that the role of marly  
435 beds is better accounted for by referring to other parameters ( $\sum t_m/T$  and  $N_m/T$ , chapters 5.1 and 5.2).

436 We conclude that while the composition of calcareous-marly beds can be neglected when  
437 assessing the role of rock composition on the bulk deformation style, the variable composition of the  
438 calcareous beds does play a role. This is accounted for by the two endmembers proposed for our  
439 multilayer succession.

440

#### 441 5.4 Geometry of folds and thrusts

442 Our field observations constrain the geometrical relationships between the attitude of minor  
443 thrusts and the orientation of folded beds with respect to the imposed stress field during shortening.  
444 We consider the variation of the angle between bedding-parallel minor thrusts developed along the  
445 fold back limbs ( $\alpha$ ; Fig. 11c) and the steeply dipping forelimbs ( $\beta$ ; Fig. 11d). This angle progressively  
446 increases as a fold tightens and amplifies during its continuous evolution, eventually leading to fold  
447 asymmetry and vergence. We note that in our field case study:

- 448 •  $\alpha$  is quite constant throughout the structural domains, and rarely exceeds  $40^\circ$  (Fig. 4a), with  
449 an average of  $\sim 36^\circ$  (Fig. 11c).
- 450 •  $\beta$  exhibits a greater variability (Fig. 11d), varying between  $34^\circ$  and  $90^\circ$  (for the upright  
451 folds), with an average of  $\sim 65^\circ$ , due to the progressive steepening of forelimbs. In the  
452 overturned folds,  $\beta$  ranges between  $50^\circ$  and  $85^\circ$ , defining an average value of  $\sim 73^\circ$  (Fig.  
453 11d).
- 454 •  $\delta$  is comparable in the hanging wall, thrust zone and footwall domains (Fig. 11e), rarely  
455 exceeding  $45^\circ$  and with an average value of  $36^\circ$ .

456 In summary,  $\delta$  and  $\alpha$  share similar values between 30° and 35° throughout the hanging wall,  
457 thrust zone and footwall domains (Fig. 11c and e).  $\delta$  and  $\beta$  are, instead, very different from each other,  
458 with a dip angle average of 35° for  $\delta$  and 60° - 73° for  $\beta$  (Fig. 11d and e).

459

## 460 **6. Discussion**

### 461 **6.1 A conceptual deformation model**

462 By integrating field observations and the semiquantitative approach illustrated above, we now  
463 propose a conceptual deformation model for the structural evolution of a carbonate multilayer  
464 succession from its undeformed stage (Figs. 12a and 13a), through an intermediate folding phase  
465 (Figs. 12b-c and 13b-c) to a final faulting stage (Figs. 12d and 13d). We discuss the evolution of the  
466 studied structures through time to highlight the progressive activation/deactivation of the studied  
467 deformation processes. We apply the conceptual evolutionary model to the Scaglia Rossa and  
468 Maiolica endmembers. Their differences notwithstanding, both deformation models take on from  
469 similar evolutions during the first increments of deformation and are described in the following  
470 conceptual steps of the progressive deformation:

- 471 • *Layer parallel shortening, layer buckling and layer parallel shearing (LPS)*

472 Deformation begins with layer parallel shortening eventually causing buckling of the  
473 succession (e.g., Whitaker and Bartholomew, 1999; Marques, 2008; Tavarnelli et al.,  
474 2021). This induces pervasive pressure solution along solution planes at high angle to  
475 bedding (Figs. 5, 12b and 13b). Layer parallel shearing (LPS), on the other hand, governs  
476 the first increments of slip along bed-bed interfaces and causes bedding planes to act as  
477 early thrust surfaces (Figs. 9, 12b and 13b; e.g., Ez, 2000; Hudleston and Treagus, 2010)  
478 as they become optimally oriented during compression. LPS, therefore, marks the  
479 transition into non-coaxial deformation from buckling.

- 480 • *Folding*

481 The second stage of deformation is represented by the more advanced folding of the  
482 multilayer succession (Figs. 12c and 13c). We consider this folding stage as encompassing  
483 all those processes that lead to the progressive increase of fold asymmetry as folds  
484 progressively evolve from the early symmetric buckle geometry during continued  
485 shortening.

486 The increase of the fold asymmetry within the folded multilayer implies a transition from  
487 pure shear to simple shear under the same stress field boundary conditions. This transition  
488 is commonly associated with rheological contrasts between the layers (Skjernaa, 1979)  
489 and/or with the original misorientation between the bedding (the studied succession) and  
490 the main fault zone (BT-SCTZ), that cuts across the multilayer (Sanderson, 1979, Casey  
491 and Huggenberger, 1985; Rowan and Kligfield, 1992), and with flexural slip processes  
492 (Ramsay, 1974; Hudleston and Treagus, 2010). Our observations indicate that early buckle  
493 folds (Figs. 5c, 12c and 13c) pass to asymmetric (Fig. 9f) and tight (Fig. 6d) geometries  
494 through the steepening of the forelimbs (Figs. 12c and 13c). This increase of asymmetry  
495 is accompanied by flexural slip for both the Scaglia Rossa and Maiolica type scenarios.  
496 Flexural slip within the Maiolica type ( $N_m/T = 1 \text{ m}^{-1}$ ; Fig. 13c) localises principally along  
497 the marly beds, whereas within the Scaglia Rossa type ( $N_m/T = 3 \text{ m}^{-1}$ ; Fig. 12c) is  
498 volumetrically distributed.

499 The two models start to behave differently only during the final phases of this stage of  
500 deformation (Figs. 12c and 13c). The Scaglia Rossa type accommodates the progressive  
501 steepening and overturning of the forelimbs (Fig. 12c), whereas the Maiolica type  
502 develops vertical and only rarely overturned fold forelimbs (Fig. 13c). Moreover, fold  
503 hinges of the Maiolica type model undergo progressive volume increase due to the flow  
504 of marls from the limbs during the initial stages of folding (Ramsay, 1967, 1974).

505

506 • *Faulting and cataclasis*

507 This stage of deformation (Figs. 12d and 13d) is accommodated by thrusting, which occurs  
508 after folds become locked-up due to their inability to accommodate further shortening by  
509 folding (e.g., Tavarnelli, 1997; Ramsay, 1974; Fischer et al., 1992). New thrusts form and  
510 localise along bed-bed interfaces on the fold back limbs (where  $\delta \sim \alpha$ ) and are driven by  
511 layer parallel shortening (Figs. 12d and 13d). Thrust surfaces cut across the verticalised or  
512 overturned forelimbs (where  $\beta \gg \delta$ ), while LPS occurs on suitably oriented back limbs  
513 (Figs. 12d and 13d) until after the folding-faulting transition. The observed thrusts are  
514 compatible with what has been previously described as “*long limb thrust*” or “*long limb*  
515 *detachment*” (e.g., Alonso and Teixell, 1992; Marques et al., 2010), which are indeed  
516 discrete slip surfaces that are sub-parallel to gently dipping limb and cut steeply-dipping  
517 or verticalised limb within asymmetric folds. For both the Maiolica and Scaglia Rossa  
518 types, faults slip first on the back limb, because of continuous folding-related flexural slip  
519 (Figs. 12d and 13d), and subsequently cut the steeply dipping limb.

520 The two endmember models strongly differ significantly in the faulting stage.  
521 Deformation is strongly distributed within the Scaglia Rossa type and only localises within  
522 the calcareous portions of the succession, where cataclasites locally develop. A foliation  
523 may form within the marly portions, cutting and transposing the verticalised or overturned  
524 fold forelimbs (Figs. 10d-e and 12d). According to Tavarnelli (1997, 2021), the thrust  
525 cutting across the forelimb progressively widens after initial localisation due to the  
526 progressive coalescence of multiple subsidiary fault planes. While these subsidiary faults  
527 develop (Fig. 12d), the thicker marly beds tend to become foliated and to wrap around  
528 calcareous lithons (Figs. 10d and f, 12d).

529 The Maiolica type model, instead, behaves differently due to the preponderance of  
530 limestone ( $\sum t_m/T = 10\%$ ,  $N_m/T = 1\text{ m}^{-1}$ ; Fig. 13d). Limestones deform by fracturing and  
531 localised cataclastic flow that are genetically associated with foreland-directed thrust  
532 propagation. The increase of deformation along thrusts is accompanied by the evolution



533 of cataclastic textures, which pass from proto- to ultra cataclasites (e.g., [Billi, 2010](#);  
534 [Ferraro et al., 2018](#)) decorating the thrust planes between the calcareous beds ([Figs. 9b-c](#)  
535 [and 13d](#)). Cataclasites may locally develop a weak foliation, particularly where the marly  
536 domains are affected ([Fig. 13d](#)). However, cataclasis is exclusively localised on the  
537 forelimbs ([Figs. 12d and 13d](#)), where thrusts cut the verticalized limbs at a high cut-off  
538 angle.

539 In both endmember cases, after the beginning of faulting, deformation on the back limbs  
540 continues to be accommodated by LPS ([Figs. 12d and 13d](#)) with thrusts and reverse faults  
541 continuing to localise along bed-bed interfaces.

542

## 543 **6.2 Constraining the activation of folding-faulting transition**

544 We have calculated the critical dip angle of fold forelimbs beyond which faulting takes over  
545 from folding. Our analysis relies on the study and quantification of 84 folds for which we have  
546 systematically measured  $\alpha$  and  $\beta$  ([Figs. 11c and d, 14a](#)). We propose a new type of plot, which shows  
547 the variation of  $\beta$  vs. the  $\beta/\alpha$  ratio ([Fig. 14a](#)), which expresses the overall fold asymmetry. 52 readings  
548 of unfaulted folds plot in a discrete cluster, with  $\beta < 80^\circ$  and  $\beta/\alpha < 1.8$  (82 % of the unfaulted folds)  
549 and form the low asymmetry fold cluster (upper two green folds in [Fig. 14b](#)). The remaining 9  
550 readings (18 %) of the unfaulted folds are characterised by  $\beta/\alpha$  values up to 3.3 ([Fig. 14a](#)), marking  
551 the transition to significant fold asymmetry (lowermost green fold in [Fig. 14b](#)).

552 The second cluster is represented by the faulted folds ([Fig. 11d](#)) with upright limbs, with  $\beta \geq 80^\circ$   
553 and  $\beta/\alpha \geq 3.3$  ([Fig. 14a](#)), testifying to a progressive verticalisation of the forelimbs and a related  
554 increase of the fold asymmetry (light blue folds in [Fig. 14b](#)). One less well-defined cluster is formed  
555 by the overturned faulted folds ([Fig. 14a](#)). Due to the progressive overturning of the forelimbs (orange  
556 folds in [Fig. 14b](#)), both  $\beta$  and  $\beta/\alpha$  values tend to decrease.  $\beta$  shows here a greater dispersion ( $50 - 85^\circ$ )

557 with respect to the upright folds (Fig. 14a and b), whereas the  $\beta/\alpha$  ratio is generally  $\geq 1.8$ , partially  
558 overlapping the folding domain (Fig. 14a).

559 We also consider the normal distribution and frequency of  $\beta$  for 28 faulted folds (Fig. 14c).  
560 Considering the upright faulted folds (light blue),  $\sim 80\%$  of the readings of  $\beta$  lie within the  $83^\circ$ - $90^\circ$   
561 interval (Fig. 14c), whereas  $\beta$  of the overturned folds shows a more dispersed pattern (Fig. 14c),  
562 ranging from  $50^\circ$  to  $87^\circ$ . The normal distribution of  $\beta$  for the upright faulted folds shows an average  
563 of  $\sim 83^\circ$  (Fig. 14c), consistent with Fig. 14a, while an average of  $\sim 73^\circ$  (Fig. 14c) represents the  
564 normal distribution of  $\beta$  for the overturned folds.

565 To sum up, our quantification demonstrates that  $\alpha$  and  $\beta$  are appropriate geometrical parameters  
566 to describe the conditions whereby the transition from folding to faulting occurs during progressive  
567 shortening. In particular,  $\beta$  close to  $80^\circ$  and  $\beta/\alpha \geq 3.3$  are critical threshold values to enable the  
568 beginning of thrusting from mature folding (Figs. 12, 13 and 14). Once the threshold is reached,  
569 thrusts form, propagate, and cut across the verticalised or overturned forelimbs (Fig. 14b). Thus, our  
570 model postulates that fold asymmetry (as neatly expressed by the  $\beta/\alpha$  ratio) is key in steering  
571 deformation, in agreement with insights from numerical modelling, where faulting is favoured as fold  
572 asymmetry increases (e.g., Simpson, 2009; Humair et al., 2020).

573

### 574 **6.3 Implications on deformation style and seismic behaviour**

575 When combined with considerations on the rock types forming the deformed multilayer, the  
576 definition of a critical limb dip angle to faulting ( $\sim 80^\circ$ ) has strong implications upon the  
577 understanding of the deformation style and seismic behaviour in fold-and-thrust belts, which we  
578 discuss here by referring to the conceptual scheme of Figure 15. Our results show that during folding  
579 (when  $\beta < 80^\circ$  and  $\beta/\alpha < 3.3$ ) carbonate multilayers may deform aseismically (Fig. 15a), with  
580 deformation being mostly accommodated by flexural slip along weak (marly) bed-bed interfaces (Fig.

581 15a). Upon reaching the critical  $\beta = 80^\circ$  and  $\beta/\alpha = 3.3$  values (time  $t_1$ , Fig. 15b), however, forelimbs  
582 lock up and begin to store stress according to a “stick” mechanical behaviour (Brace and Byerlee,  
583 1966; Fig. 15b). Layer parallel shearing remains active in the back limbs (Fig. 15b), which  
584 accommodate strain aseismically by exploiting the weak marly beds of the deforming multilayer (Fig.  
585 15b). Coseismic rupturing (“slip” behaviour, Brace and Byerlee, 1966; time  $t_2$  in Fig. 15b) eventually  
586 localises when the rock strength in the forelimbs is finally overcome and a discrete Principal Slip  
587 Surface forms (PSS; Fig. 15b). At this stage, folds are “deactivated”, decapitated by thrusts, and  
588 further deformation is taken up exclusively by discrete localised faulting. The overall rheology of the  
589 system becomes thus governed by the mechanics of the newly formed fault, whereas, on the back  
590 limbs, strain is continuously accommodated by aseismic layer parallel shearing (Fig. 15c). Cyclically,  
591 continuous shortening will lead to critical conditions for renewed seismic rupturing (time  $t_3, t_4, t_n$ )  
592 along the thrust surfaces. For each coseismic rupture, thrusts may widen, for example by the  
593 formation and coalescence of cataclasites (Fig. 15c).

594 In summary, during and after the folding-faulting transition (Figs. 12d, 13d, 15), the system we  
595 describe can simultaneously host two different styles of deformation: i) discrete brittle deformation  
596 along discrete thrusts accompanied by seismic rupturing on the forelimbs (Fig. 15c), which, upon  
597 continuous shortening, end up being highly misoriented to the imposed stress field (Figs. 9b-d and  
598 10d-e), and ii) aseismic creep on suitably oriented back limbs, (Figs. 12d, 13d, 15), which forms  
599 variably-sized foliated domains within the marly parts of the deforming multilayer succession (Fig.  
600 10f).

601

## 602 6.4 Upscaling of the deformation model

603 Our conceptual deformation model and its implications on seismic behaviour are of great  
604 potential interest when considering the seismotectonic framework and the seismic hazard of active  
605 fold-and-thrust belts deforming carbonate multilayer successions, like the ESA. The up-scaled

606 applicability of the results derived in this study obviously needs to be thoroughly investigated and  
607 validated against real case scenarios where geophysical data are of sufficient quality to allow exact  
608 spatial correlations between earthquake hypocentres and the geometry of folds and thrusts. To that  
609 end, however, we first need to assess whether our results are (meso)scale-dependent or can instead  
610 be extrapolated to the much larger dimensions of entire belts. Our model relies on numerical ratios  
611 (i.e.,  $\sum t_m/T$ ,  $N_m/T$ ) and values (i.e.,  $\alpha$ ,  $\beta$ ,  $\delta$  and  $\beta/\alpha$  ratio) that are used to characterise rock type and  
612 structural geometry, respectively. These are dimensionless parameters, such that they can also be used  
613 to describe thicker (km-thick) multilayer successions or to characterise the geometrical relationships  
614 between back- and forelimbs aiming to constrain the evolution of km-scale folds.

615 The possibility to upscale our findings is also justified by the cyclic nature of sedimentation  
616 within carbonate multilayer successions. This cyclicity, which principally reflects recurrent and  
617 periodic environmental changes during sedimentation, is documented by the interbedding of  
618 terrigenous- (e.g., marl) and calcareous- beds/units, and is present at all scales of observation due to  
619 different temporal amplitudes of the sedimentation cycles (i.e., from hundreds of My to hundreds of  
620 ky). In this scenario, the interlayering of pure calcareous and marly formations (e.g., reflecting  
621 temporal cycles on the hundreds of My scale) represents the effects of high-amplitude sedimentation  
622 cycles, whereas the interlayering of mesoscale beds represents the effects of low- amplitude cycles  
623 (e.g., hundreds of ky). As described above, multilayer carbonate successions share similar  
624 stratigraphic and architectural features at different scales of observation, confirming that our  
625 parametric approach can be readily applied to also thicker successions.

626 Lastly, our results are applicable in different geological contexts if we consider our system as an  
627 analogue of a “standard” carbonate pelagic succession, composed of several sedimentary cycles. All  
628 local heterogeneities notwithstanding, the described succession can be considered as an appropriate  
629 mechanical analogue of carbonate multilayer successions elsewhere, irrespective of stratigraphic age  
630 (Neoproterozoic, Oman Mountains, [Allen, 2007](#); Mesozoic, Lesser Caucasus, [Gusmeo et al., 2021](#);

631 Palaeozoic – Cenozoic, Western Alps, [Decarlis et al., 2013](#); Meso – Cenozoic, Central Apennines,  
632 [Fabbi, 2014](#); [Cipriani, 2019](#)). For instance, the specific sedimentological and architectural features of  
633 the analysed succession ([Fig. 3c](#)) are representative of many successions associated with rifting  
634 related to the opening of the Tethyan Ocean, now exposed in several peri-Mediterranean areas and in  
635 fold-and-thrust belts moving from Cuba to Japan (e.g., [Wieczorek, 1988](#); [Masse et al., 1995](#); [Bernoulli](#)  
636 [and Jenkyns, 2009](#)).

637

## 638 **7. Conclusions**

639 The carbonate multilayer succession affected by the San Donato-Costa Thrust Zone (Eastern  
640 Southern Alps of Italy) has allowed us to explore and constrain the parameters that govern the folding-  
641 faulting transition during shortening in carbonate multilayer successions. Our data confirm that the  
642 mechanical stratigraphy of the deforming multilayer plays a key role in governing the bulk style of  
643 deformation and deformation partitioning in the carbonate and marly endmembers of compositionally  
644 heterogeneous multilayers. Deformation progresses from i) layer parallel shortening, layer parallel  
645 shearing and incipient buckling, through ii) buckling and folding, to iii) faulting and cataclasis. Our  
646 conceptual evolutionary model suggests that this evolution is accommodated by fold amplification  
647 and increasing asymmetry until post-folding faulting activates. For the first time, we quantitatively  
648 determined a critical angle threshold for the transition from folding to faulting, which we link to the  
649 progressive increase of the dip angle of back limbs ( $\alpha$ ) and forelimbs ( $\beta$ ). This threshold, which  
650 corresponds to  $\beta \geq 80^\circ$  and  $\beta/\alpha \geq 3.3$ , represents the condition for faulting to take over from folding  
651 in a multilayer carbonate-dominated succession.

652 This purely geometrical set of constraints is intrinsically scale-independent and can, therefore,  
653 be applied to the scale of an entire fold-and-thrust-belt aiming at exploring, for example, the  
654 geometrical-structural conditions that control hypocentre location within a seismically deforming  
655 carbonate multilayer succession. Insights from this study help to improve our understanding of

656 distributed deformation localisation and seismic rupturing and may prove useful to better assess the  
657 seismotectonic framework and seismic hazard of active fold-and-thrust belts affecting multilayer  
658 carbonate successions.

## 659 **Acknowledgments**

660 The authors thank Francesca Stendardi for her support in the field. Angelo Cipriani is thanked for the  
661 fruitful discussion about the stratigraphy of the area. Alberto Ceccato is thanked for his support and  
662 the discussion concerning the data analysis. The present work benefited from the fruitful and  
663 constructive reviews of two anonymous reviewers. We thank Fabrizio Agosta for the editorial  
664 handling and for useful comments on the final version of the manuscript.

665

## 666 **Funding**

667 This work belongs to the PhD project “Structural characterisation of selected thrust zones in the  
668 Eastern Southern Alps and Northern Oman: implication on strain localisation and seismogenesis in  
669 carbonates” of the first author.

670

## 671 **Reference**

672 Allen, P. A., 2007. The Huqf Supergroup of Oman: basin development and context for Neoproterozoic  
673 glaciation. *Earth-Science Reviews* 84(3-4), 139-185. <http://dx.doi.org/10.1016/j.earscirev.2007.06.005>.

674 Alonso, J., L. & Teixell, A., 1992. Forelimb deformation in some natural examples of fault-propagation folds.  
675 In: *Thrust tectonics*. Springer, Dordrecht, 1992. 175-180. [https://doi.org/10.1007/978-94-011-3066-  
676 0\\_15](https://doi.org/10.1007/978-94-011-3066-0_15).

677 Anderlini, L., Serpelloni, E., Tolomei, C., Marco De Martini, P., Pezzo, G., Gualandi, A., and Spada, G., 2020.  
678 New insights into active tectonics and seismogenic potential of the Italian Southern Alps from vertical  
679 geodetic velocities. *Solid Earth* 11, 1681–1698. <https://doi.org/10.5194/se-11-1681-2020>.

680 Anselmi, M., Govoni, A., De Gori, P., and Chiarabba, C., 2011. Seismicity and velocity structures along the  
681 south-Alpine thrust front of the Venetian Alps (NE-Italy). *Tectonophysics* 513, 37–48.  
682 <https://doi.org/10.1016/j.tecto.2011.09.023>.

683 Beaudoin, N., Bellahsen, N., Lacombe, O., Emmanuel, L., and Pironon, J., 2014. Crustal- scale fluid flow  
684 during the tectonic evolution of the Bighorn Basin (Wyoming, USA). *Basin Research* 26(3), 403-435.  
685 <http://dx.doi.org/10.1111/bre.12032>.

686 Bernoulli, D., and Jenkyns, H. C., 2009 . Ancient oceans and continental margins of the Alpine-Mediterranean  
687 Tethys: Deciphering clues from Mesozoic pelagic sediments and ophiolites. *Sedimentology* 56(1), 149–  
688 190. <https://doi.org/10.1111/j.1365-3091.2008.01017.x>.

689 Bigi, S., Pisani, P. C., Tavarnelli, E., Calamita, F., & Paltrinieri, W., 2003. The " pre-thrusting" Fiamignano  
690 normal fault. *Bollettino della Società geologica italiana* 122(2), 267-276.

691 Billi, A., Salvini, F., and Storti, F., 2003. The damage zone-fault core transition in carbonate rocks:  
692 implications for fault growth, structure and permeability. *Journal of Structural geology* 25(11), 1779-  
693 1794. [https://doi.org/10.1016/S0191-8141\(03\)00037-3](https://doi.org/10.1016/S0191-8141(03)00037-3).

694 Billi, A., 2010. Microtectonics of low-P low-T carbonate fault rocks. *Journal of Structural Geology* 32(9),  
695 1392-1402. <https://doi.org/10.1016/j.jsg.2009.05.007>.

696 Bosellini, A., Masetti, D., and Sarti, M., 1981. A Jurassic ‘tongue of the ocean’ infilled with oolitic sands: The  
697 Belluno Trough, Venetian Alps, Italy. *Marine Geology* 44(1–2),  
698 59–95. [https://doi.org/10.1016/0025-3227\(81\)90113-4](https://doi.org/10.1016/0025-3227(81)90113-4).

699 Bosellini, A., Gianolla, P., & Stefani, M., 2003. Geology of the Dolomites. *Episodes* 26(3), 181-185.  
700 <https://doi.org/10.18814/epiugs/2003/v26i3/005>.

701 Brace, W. F., and Byerlee, J. D., 1966. Stick-slip as a mechanism for earthquakes. *Science* 153(3739), 990-  
702 992. <https://doi.org/10.1126/science.153.3739.990>.

703 Bullock, R.J., De Paola, N., Holdsworth, R.E., and Trabucho-Alexandre, J., 2014. Lithological controls on the  
704 deformation mechanisms operating within carbonate-hosted faults during the seismic cycle: *Journal of*  
705 *Structural Geology* 58, 22–42. <https://doi.org/10.1016/j.jsg.2013.10.008>.

706 Butler, R. W., Maniscalco, R., and Pinter, P. R., 2019. Syn-kinematic sedimentary systems as constraints on  
707 the structural response of thrust belts: re-examining the structural style of the Maghrebian thrust belt of  
708 Eastern Sicily. *Italian Journal of Geosciences* 138(3), 371-389. <https://doi.org/10.3301/IJG.2019.11>.

709 Butler, R.W.H., Bond, C.E., Cooper, M.A., and Watkins, H., 2020. Fold–thrust structures – Where have all  
710 the buckles gone? *Geological Society Special Publication* 487, 21–44. <https://doi.org/10.1144/SP487.7>.

711 Caputo, R., Poli, M.E., Zanferrari, A., 2010. Neogene-Quaternary tectonic stratigraphy of the eastern Southern  
712 Alps, NE Italy. *Journal of Structural Geology* 32, 1009-1027.  
713 <http://dx.doi.org/10.1016/j.jsg.2010.06.004>.

714 Carminati, E., Doglioni, C., and Scrocca, D., 2004. Alps Vs Apennines: Special Volume of the Italian  
715 Geological Society, 141–151.

716 Carminati, E., Enzi, S., and Camuffo, D., 2007. A study on the effects of seismicity on subsidence in foreland  
717 basins: An application to the Venice area: *Global and Planetary Change* 55, 237–250.  
718 <https://doi.org/10.1016/j.gloplacha.2006.03.003>.

719 Carminati, E., Aldega, L., Trippetta, F., and Kavooosi, M.A., 2018. Zagros fold and thrust belt in the Fars  
720 province (Iran) I: Control of thickness/rheology of sediments and pre-thrusting tectonics on structural  
721 style and shortening. *Marine and Petroleum Geology* 91, 211-224.  
722 <https://doi.org/10.1016/j.marpetgeo.2018.01.005>.

723 Casey, M., & Huggenberger, P., 1985. Numerical modelling of finite-amplitude similar folds developing under  
724 general deformation histories. *Journal of Structural Geology* 7(1), 103-114.  
725 [https://doi.org/10.1016/0191-8141\(85\)90118-X](https://doi.org/10.1016/0191-8141(85)90118-X).

726 Castellarin, A., Lucchini, F., Rossi, P. L., Selli, L., and Simboli, G., 1988. The Middle Triassic magmatic-  
727 tectonic arc development in the Southern Alps. *Tectonophysics* 146(1-4), 79-89.  
728 [https://doi.org/10.1016/0040-1951\(88\)90083-2](https://doi.org/10.1016/0040-1951(88)90083-2).

729 Castellarin, A., and Cantelli, L., 2000. Neo-Alpine evolution of the Southern Eastern Alps. *Journal of*  
730 *Geodynamics* 30, 251–274. [https://doi.org/10.1016/S0264-3707\(99\)00036-8](https://doi.org/10.1016/S0264-3707(99)00036-8).

731 Castellarin, A., Nicolich, R., Fantoni, R., Cantelli, L., Sella, M., and Selli, L., 2006. Structure of the lithosphere





757 M. D., Looser, N., & Carminati, E., 2021. U-Pb age of the 2016 Amatrice earthquake causative fault  
758 (Mt. Gorzano, Italy) and paleo-fluid circulation during seismic cycles inferred from inter-and co-seismic  
759 calcite. *Tectonophysics* 819, 229076. <http://dx.doi.org/10.1016/j.tecto.2021.229076>.

760 Dautriat, J., Bornert, M., Gland, N., Dimanov, A., & Raphanel, J. 2011. Localized deformation induced by  
761 heterogeneities in porous carbonate analysed by multi-scale digital image  
762 correlation. *Tectonophysics* 503(1-2), 100-116. <https://doi.org/10.1016/j.tecto.2010.09.025>.

763 D'Alberto, L., Boz, A., and Doglioni, C., 1995. Structure of the Vette Feltrine (Eastern Southern  
764 Alps). *Memorie Della Società Geologica Italiana* 47, 189–199.

765 D'Ambrogi, C., and Doglioni, C., 2008. Struttura delle Vette Feltrine. *Rendiconti Online Società Geologica*  
766 *Italiana* 4, 37–40.

767 De Min, A., Velicogna, M., Ziberna, L., Chiaradia, M., Alberti, A., & Marzoli, A., 2020. Triassic magmatism  
768 in the European Southern Alps as an early phase of Pangea break-up. *Geological Magazine* 157(11),  
769 1800-1822. <https://doi.org/10.1017/S0016756820000084>.

770 Decarlis, A., Dallagiovanna, G., Lualdi, A., Maino, M., & Seno, S., 2013. Stratigraphic evolution in the  
771 Ligurian Alps between Variscan heritages and the Alpine Tethys opening: A review. *Earth-Science*  
772 *Reviews* 125, 43-68. <https://doi.org/10.1016/j.earscirev.2013.07.001>.

773 Delle Piane, C., Clennell, M. B., Keller, J. V., Giwelli, A., and Luzin, V., 2017. Carbonate hosted fault rocks:  
774 A review of structural and microstructural characteristic with implications for seismicity in the upper  
775 crust. *Journal of Structural Geology* 103, 17-36. <https://doi.org/10.1016/j.jsg.2017.09.003>.

776 Doglioni, C., 1987. Tectonic of the Dolomites (Southern Alps, Northern Italy). *Journal of Structural Geology*  
777 9, 181–193. [https://doi.org/10.1016/0191-8141\(87\)90024-1](https://doi.org/10.1016/0191-8141(87)90024-1).

778 Doglioni, C., 1990. Thrust tectonic examples from the Venetian Alps. *Studi Geologici Camerti*, 117-129.

779 Doglioni, C., 1992. The Venetian Alps thrust belt. In *Thrust tectonics* (319-324). Springer, Dordrecht.

780 Doglioni, C., and Carminati, E., 2008. Structural styles and Dolomites field trip. *Memorie Descrittive della*  
781 *Carta Geologica d'Italia* 82, 1–299.

782 Erickson, S.G., 1996. Influence of mechanical stratigraphy on folding vs faulting. *Journal of Structural*  
783 *Geology* 18, 443–450. [https://doi.org/10.1016/0191-8141\(95\)00064-K](https://doi.org/10.1016/0191-8141(95)00064-K).

784 Ez, V., 2000. When shearing is a cause of folding. *Earth-Science Reviews* 51(1-4), 155-172.  
785 [https://doi.org/10.1016/S0012-8252\(00\)00020-9](https://doi.org/10.1016/S0012-8252(00)00020-9).

786 Fabbi, S., 2014. Geology and Jurassic paleogeography of the Mt. Primo-Mt. Castel Santa Maria ridge and  
787 neighbouring areas (Northern Apennines, Italy). *Journal of Maps* 11(4), 645-663.  
788 <https://doi.org/10.1080/17445647.2014.956235>.

789 Fagereng, Å., Hillary, G. W., and Diener, J. F., 2014. Brittle- viscous deformation, slow slip, and  
790 tremor. *Geophysical Research Letters* 41(12), 4159-4167. <http://dx.doi.org/10.1002/2014GL060433>.

791 Ferraro, F., Grieco, D. S., Agosta, F., & Prosser, G., 2018. Space-time evolution of cataclasis in carbonate fault  
792 zones. *Journal of Structural Geology* 110, 45-64. <https://doi.org/10.1016/j.jsg.2018.02.007>.

793 Fischer, M.P., Woodward, N.B., and Mitchell, M.M., 1992. The kinematics of break-thrust folds. *Journal of*  
794 *Structural Geology* 14, 451–460. [https://doi.org/10.1016/0191-8141\(92\)90105-6](https://doi.org/10.1016/0191-8141(92)90105-6).

795 Fischer, M.P., and Jackson, P.B., 1999. Stratigraphic controls on deformation patterns in fault-related folds: A  
796 detachment fold example from the Sierra Madre Oriental, northeast Mexico. *Journal of Structural*  
797 *Geology* 21, 613–633. [https://doi.org/10.1016/S0191-8141\(99\)00044-9](https://doi.org/10.1016/S0191-8141(99)00044-9).

798 Fossen, H., 2016. *Structural geology*. Cambridge university press.

799 Galadini, F., Poli, M.E., and Zanferrari, A., 2005. Seismogenic sources potentially responsible for earthquakes  
800 with  $M \geq 6$  in the Eastern Southern Alps (Thiene-Udine sector, NE Italy). *Geophysical Journal*  
801 *International* 161, 739–762. <https://doi.org/10.1111/j.1365-246X.2005.02571.x>.

802 Giorgetti, C., Collettini, C., Scuderi, M.M., Barchi, M.R., and Tesei, T., 2016. Fault geometry and mechanics  
803 of marly carbonate multilayers: An integrated field and laboratory study from the Northern Apennines,  
804 Italy. *Journal of Structural Geology* 93, 1–16, <https://doi.org/10.1016/j.jsg.2016.10.001>.

805 Gusmeo, T., Cavazza, W., Alania, V. M., Enukidze, O. V., Zattin, M., & Corrado, S., 2021. Structural inversion  
806 of back-arc basins–The Neogene Adjara-Trialeti fold-and-thrust belt (SW Georgia) as a far-field effect

807 of the Arabia-Eurasia collision. *Tectonophysics* 803, 228702.  
808 <https://doi.org/10.1016/j.tecto.2020.228702>.

809 Handy, M. R., Schmid, S. M., Bousquet, R., Kissling, E., and Bernoulli, D., 2010. Reconciling plate-tectonic  
810 reconstructions of Alpine Tethys with the geological–geophysical record of spreading and subduction  
811 in the Alps. *Earth-Science Reviews* 102(3-4), 121-158. <https://doi.org/10.1016/j.earscirev.2010.06.002>.

812 Hudleston, P.J., Treagus, S.H., and Lan, L., 1996. Flexural flow folding: Does it occur in nature? *Geology* 24,  
813 203–206. [https://doi.org/10.1130/0091-7613\(1996\)024%3C0203:FFFDIO%3E2.3.CO;2](https://doi.org/10.1130/0091-7613(1996)024%3C0203:FFFDIO%3E2.3.CO;2).

814 Hudleston, P.J., and Treagus, S.H., 2010. Information from folds: A review. *Journal of Structural Geology* 32,  
815 2042–2071, <https://doi.org/10.1016/j.jsg.2010.08.011>.

816 Humair, F., Bauville, A., Epard, J.L., and Schmalholz, S.M., 2020. Interaction of folding and thrusting during  
817 fold-and-thrust-belt evolution: Insights from numerical simulations and application to the Swiss Jura  
818 and the Canadian Foothills. *Tectonophysics* 789, 228474, <https://doi.org/10.1016/j.tecto.2020.228474>.

819 Ikari, M. J., Niemeijer, A. R., & Marone, C., 2015. Experimental investigation of incipient shear failure in  
820 foliated rock. *Journal of Structural Geology* 77, 82-91. <https://doi.org/10.1016/j.jsg.2015.05.012>.

821 ISIDe Working Group, 2007. Italian Seismological Instrumental and Parametric Database (ISIDe). Istituto  
822 Nazionale di Geofisica e Vulcanologia (INGV). <http://doi.org/10.13127/ISIDE>.

823 Kamb, W. B., 1959. Ice petrofabric observations from Blue Glacier, Washington, in relation to theory and  
824 experiment. *Journal of Geophysical Research* 64(11), 1891-1909.  
825 <https://doi.org/10.1029/JZ064i011p01891>.

826 Kilian, R., Heilbronner, R., and Stünitz, H., 2011. Quartz grain size reduction in a granitoid rock and the  
827 transition from dislocation to diffusion creep. *Journal of Structural Geology* 33, 1265–1284.  
828 <https://doi.org/10.1016/j.jsg.2011.05.004>.

829 Kilian, S., Ortner, H., and Schneider-Muntau, B., 2021. Buckle folding in the Northern Calcareous Alps-Field  
830 observations and numeric experiments. *Journal of Structural Geology* 150, 104416.  
831 <https://doi.org/10.1016/j.jsg.2021.104416>.

- 832 Labaume, P., Carrio-Schaffhauser, E., Gamond, J. F., and Renard, F., 2004. Deformation mechanisms and  
833 fluid-driven mass transfers in the recent fault zones of the Corinth Rift (Greece). *Comptes Rendus*  
834 *Geoscience* 336(4-5), 375-383. <https://doi.org/10.1016/j.crte.2003.11.010>.
- 835 Lacombe, O., Lavé, J., Roure, F. M., & Verges, J. (Eds.), 2007a. Thrust belts and foreland basins: From fold  
836 kinematics to hydrocarbon systems. Springer Science & Business Media.
- 837 Lena, G., Barchi, M.R., Alvarez, W., Felici, F., and Minelli, G., 2015. Mesostructural analysis of S-Cfabrics  
838 in a shallow shear zone of the Umbria-Marche Apennines (Central Italy). *Geological Society Special*  
839 *Publication* 409, 149–166. <https://doi.org/10.1144/SP409.10>.
- 840 Lustrino, M., Abbas, H., Agostini, S., Caggiati, M., Carminati, E., and Gianolla, P., 2019. Origin of Triassic  
841 magmatism of the Southern Alps (Italy): Constraints from geochemistry and Sr-Nd-Pb isotopic  
842 ratios. *Gondwana Research* 75, 218-238. <http://dx.doi.org/10.1016/j.gr.2019.04.011>.
- 843 Marchesini, B., Garofalo, P. S., Menegon, L., Mattila, J., & Viola, G., 2019. Fluid-mediated, brittle–ductile  
844 deformation at seismogenic depth–Part 1: Fluid record and deformation history of fault veins in a nuclear  
845 waste repository (Olkiluoto Island, Finland). *Solid Earth* 10(3), 809-838. [https://doi.org/10.5194/se-10-](https://doi.org/10.5194/se-10-809-2019)  
846 [809-2019](https://doi.org/10.5194/se-10-809-2019).
- 847 Marques, F.O., 2008. Thrust initiation and propagation during shortening of a 2-layer model lithosphere.  
848 *Journal of Structural Geology* 30, 29–38. <https://doi.org/10.1016/j.jsg.2007.09.005>.
- 849 Marques, F. O., Burg, J.-P., Lechmann, S. M. & Schmalholz, S. M., 2010. Fluid assisted particulate flow of  
850 turbidites at very low temperature: A key to tight folding in a submarine Variscan foreland basin of SW  
851 Europe. *Tectonics* 29(2). <https://doi.org/10.1029/2008TC002439>.
- 852 Masetti, D., Claps, M., Giacometti, A., Lodi, P., and Pignatti, P., 1998. I Calcari Grigi della Piattaforma di  
853 Trento (Lias inferiore e medio, Prealpi Venete). *Atti Ticinensi Scienze della Terra* 40, 139–183.  
854 <http://hdl.handle.net/11368/1697434>.

855 Masse, J. P., Philip, J., and Camoin, G., 1995. The Cretaceous Tethys. In *The Tethys Ocean* 215-236. Springer,  
856 Boston, MA.inger, Boston, MA.

857 Micarelli, L., Benedicto, A., & Wibberley, C. A. J. 2006. Structural evolution and permeability of normal fault  
858 zones in highly porous carbonate rocks. *Journal of Structural Geology* 28(7), 1214-1227.  
859 <https://doi.org/10.1016/j.jsg.2006.03.036>.

860 Michie, E. A. H., Haines, T. J., Healy, D., Neilson, J. E., Timms, N. E., and Wibberley, C. A. J., 2014. Influence  
861 of carbonate facies on fault zone architecture. *Journal of Structural Geology* 65, 82-99.  
862 <https://doi.org/10.1016/j.jsg.2014.04.007>.

863 Michie, E.A.H., 2015. Influence of host lithofacies on fault rock variation in carbonate fault zones: A case  
864 study from the Island of Malta. *Journal of Structural Geology* 76, 61–79,  
865 <https://doi.org/10.1016/j.jsg.2015.04.005>.

866 Nabavi, S.T., and Fossen, H., 2021. Fold geometry and folding – a review. *Earth-Science Reviews*, 103-812,  
867 <https://doi.org/10.1016/j.earscirev.2021.103812>.

868 Ramsay, J. G., 1967. *Folding and fracturing of rocks*. Mc Graw Hill Book Company, 568.

869 Ramsay, J.G., 1974. Development of Chevron Folds. *Bulletin of the Geological Society of America* 85, 1741–  
870 1754. [https://doi.org/10.1130/0016-7606\(1976\)87<1664:DOCFD>2.0.CO;2](https://doi.org/10.1130/0016-7606(1976)87<1664:DOCFD>2.0.CO;2).

871 Ramsay, J.G., and Graham, R.H., 1970. Strain variation in shear belts. *Canadian Journal of Earth Sciences* 7,  
872 786–813. <https://doi.org/10.1139/e70-078>.

873 Rowan, M. G., and Kligfield, R., 1992. Kinematics of large-scale asymmetric buckle folds in overthrust shear:  
874 an example from the Helvetic nappes. In *Thrust tectonics* 165-173. [https://doi.org/10.1007/978-94-011-](https://doi.org/10.1007/978-94-011-3066-0_14)  
875 [3066-0\\_14](https://doi.org/10.1007/978-94-011-3066-0_14).

876 Ruh, J. B., Kaus, B. J., and Burg, J. P., 2012. Numerical investigation of deformation mechanics in fold- and  
877 thrust belts: Influence of rheology of single and multiple décollements. *Tectonics* 31(3).  
878 <http://dx.doi.org/10.1029/2011TC003047>.

- 879 Sanderson, D. J. 1979. The transition from upright to recumbent folding in the Variscan fold belt of southwest  
880 England: a model based on the kinematics of simple shear. *Journal of Structural Geology* 1(3), 171-180.  
881 [https://doi.org/10.1016/0191-8141\(79\)90037-3](https://doi.org/10.1016/0191-8141(79)90037-3).
- 882 Schaltegger, U., and Brack, P., 2007. Crustal-scale magmatic systems during intracontinental strike-slip  
883 tectonics: U, Pb and Hf isotopic constraints from Permian magmatic rocks of the Southern Alps.  
884 *International Journal of Earth Sciences* 96, 1131–1151. <https://doi.org/10.1007/s00531-006-0165-8>.
- 885 Schmid, S.M., Fügenschuh, B., Kissling, E., and Schuster, R., 2004. Tectonic map and overall architecture of  
886 the Alpine orogen. *Eclogae Geologicae Helvetiae* 97, 93–117. [https://doi.org/10.1007/s00015-004-](https://doi.org/10.1007/s00015-004-1113-x)  
887 [1113-x](https://doi.org/10.1007/s00015-004-1113-x).
- 888 Selli, L., 1998. Il lineamento della Valsugana fra Trento e Cima d'Asta: cinematica neogenica ed eredità  
889 strutturali permo-mesozoiche nel quadro evolutivo del Sudalpino Orientale (NE-Italia). *Memorie della*  
890 *Società Geologica Italiana* 53, 503-541.
- 891 Serpelloni, E., Vannucci, G., Anderlini, L., and Bennett, R.A., 2016. Kinematics, seismotectonics and seismic  
892 potential of the eastern sector of the European Alps from GPS and seismic deformation data.  
893 *Tectonophysics* 688, 157–181. <https://doi.org/10.1016/j.tecto.2016.09.026>.
- 894 Sibson, R. H., 1994. Crustal stress, faulting and fluid flow. Geological Society, London, Special Publications  
895 78(1), 69-84. <https://doi.org/10.1144/GSL.SP.1994.078.01.07>.
- 896 Simpson, G.D.H., 2009. Mechanical modelling of folding versus faulting in brittle-ductile wedges. *Journal of*  
897 *Structural Geology* 31, 369–381. <https://doi.org/10.1016/j.jsg.2009.01.011>.
- 898 Skjervnaa, L., 1980. Rotation and deformation of randomly oriented planar and linear structures in progressive  
899 simple shear. *Journal of Structural Geology* 2(1-2), 101-109. [https://doi.org/10.1016/0191-](https://doi.org/10.1016/0191-8141(80)90039-5)  
900 [8141\(80\)90039-5](https://doi.org/10.1016/0191-8141(80)90039-5).
- 901 Smith, S.A.F., Billi, A., di Toro, G., and Spiess, R., 2011. Principal Slip Zones in Limestone: Microstructural  
902 Characterization and Implications for the Seismic Cycle (Tre Monti Fault, Central Apennines, Italy).  
903 *Pure and Applied Geophysics* 168, 2365–2393. <https://doi.org/10.1007/s00024-011-0267-5>.

- 904 Stefani, C., Fellin, M. G., Zattin, M., Zuffa, G. G., Dalmonte, C., Mancin, N., and Zanferrari, A., 2007.  
905 Provenance and paleogeographic evolution in a multi-source foreland: The Cenozoic Venetian-Friulian  
906 Basin (NE Italy). *Journal of Sedimentary Research* 77(11–12), 867–887.  
907 <https://doi.org/10.2110/jsr.2007.083>.
- 908 Stewart, I. S., and Hancock, P. L., 1991. Scales of structural heterogeneity within neotectonic normal fault  
909 zones in the Aegean region. *Journal of Structural Geology* 13(2), 191–204. [https://doi.org/10.1016/0191-](https://doi.org/10.1016/0191-8141(91)90066-R)  
910 [8141\(91\)90066-R](https://doi.org/10.1016/0191-8141(91)90066-R).
- 911 Swanson, E.M., Wernicke, B.P., Eiler, J.M., and Losh, S., 2012. Temperatures and fluids on faults based on  
912 carbonate clumped-isotope thermometry. *American Journal of Science* 312, 1–21,  
913 <https://doi.org/10.2475/01.2012.01>.
- 914 Tavani, S., Storti, F., Salvini, F., and Toscano, C., 2008. Stratigraphic versus structural control on the  
915 deformation pattern associated with the evolution of the Mt. Catria anticline, Italy. *Journal of Structural*  
916 *Geology* 30, 664–681. <https://doi.org/10.1016/j.jsg.2008.01.011>.
- 917 Tavani, S., Storti, F., Lacombe, O., Corradetti, A., Muñoz, J.A., and Mazzoli, S., 2015. A review of  
918 deformation pattern templates in foreland basin systems and fold-and-thrust belts: Implications for the  
919 state of stress in the frontal regions of thrust wedges. *Earth-Science Reviews* 141, 82–104.  
920 <https://doi.org/10.1016/j.earscirev.2014.11.013>.
- 921 Tavarnelli, E., 1997. Structural evolution of a foreland fold-and-thrust belt: The Umbria-Marche Apennines,  
922 Italy. *Journal of Structural Geology* 19, 523–534. [https://doi.org/10.1016/s0191-8141\(96\)00093-4](https://doi.org/10.1016/s0191-8141(96)00093-4).
- 923 Tavarnelli, E., Mazzarini, F., Scialoja, E., and Isola, I., 2021. Deformation history of a foredeep basin during  
924 the incorporation of its deposits within an advancing orogenic wedge: The case of the Oligocene-Early  
925 Miocene Macigno Costiero Formation, southern Tuscany, northern Apennines, Italy. *Journal of*  
926 *Structural Geology* 147, 104347. <https://doi.org/10.1016/j.jsg.2021.104347>.
- 927 Tesei, T., Collettini, C., Viti, C., and Barchi, M.R., 2013. Fault architecture and deformation mechanisms in  
928 exhumed analogues of seismogenic carbonate-bearing thrusts. *Journal of Structural Geology* 55, 167–  
929 181. <https://doi.org/10.1016/j.jsg.2013.07.007>.



930 Tondi, E., Antonellini, M., Aydin, A., Marchegiani, L., and Cello, G., 2006. The role of deformation bands,  
931 stylolites and sheared stylolites in fault development in carbonate grainstones of Majella Mountain,  
932 Italy. *Journal of Structural Geology* 28, 376–391. <https://doi.org/10.1016/j.jsg.2005.12.001>.

933 Trevisani, E., 1991. Il Toarciano-Aaleniano nei settori centro-orientali della piattaforma di Trento (Prealpi  
934 Venete). *Rivista Italiana Di Paleontologia e Stratigrafia* 97(1), 99–124.

935 Twiss, R.J. and Moores, E.M., 1992. *Structural Geology*. W.H. Freeman and Company, New York, 532.

936 Vignaroli, G., Viola, G., Diamanti, R., Zuccari, C., Garofalo, P. S., Bonini, S., and Selli, L., 2020. Multistage  
937 strain localisation and fluid-assisted cataclasis in carbonate rocks during the seismic cycle: Insights from  
938 the Belluno Thrust (eastern Southern Alps, Italy). *Journal of Structural Geology* 141, 104216.  
939 <https://doi.org/10.1016/j.jsg.2020.104216>.

940 Whitaker, A. E., & Bartholomew, M. J., 1999. Layer parallel shortening; a mechanism for determining  
941 deformation timing at the junction of the Central and Southern Appalachians. *American Journal of*  
942 *Science* 299(3), 238-254. <https://doi.org/10.2475/ajs.299.3.238>.

943 Wieczorek, J., 1988. Maiolica - a unique facies of the western Tethys. *Annales Societatis Geologorum Poloniae*  
944 58, 255–276.

945 Winterer, E.L., and Bosellini, A., 1981. Subsidence and sedimentation on Jurassic passive continental margin,  
946 southern Alps, Italy. *American Association of Petroleum Geologists Bulletin* 65, 394–421,  
947 <https://doi.org/10.1306/2f9197e2-16ce-11d7-8645000102c1865d>.

948 Zuccari, C., Vignaroli, G., and Viola, G., 2021. Geological map of the San Donato–Costa Thrust Zone, Belluno  
949 Thrust System, eastern Southern Alps (northern Italy). *Journal of Maps* 17(2), 337-347.  
950 <http://dx.doi.org/10.1080/17445647.2021.1946444>.

951

952

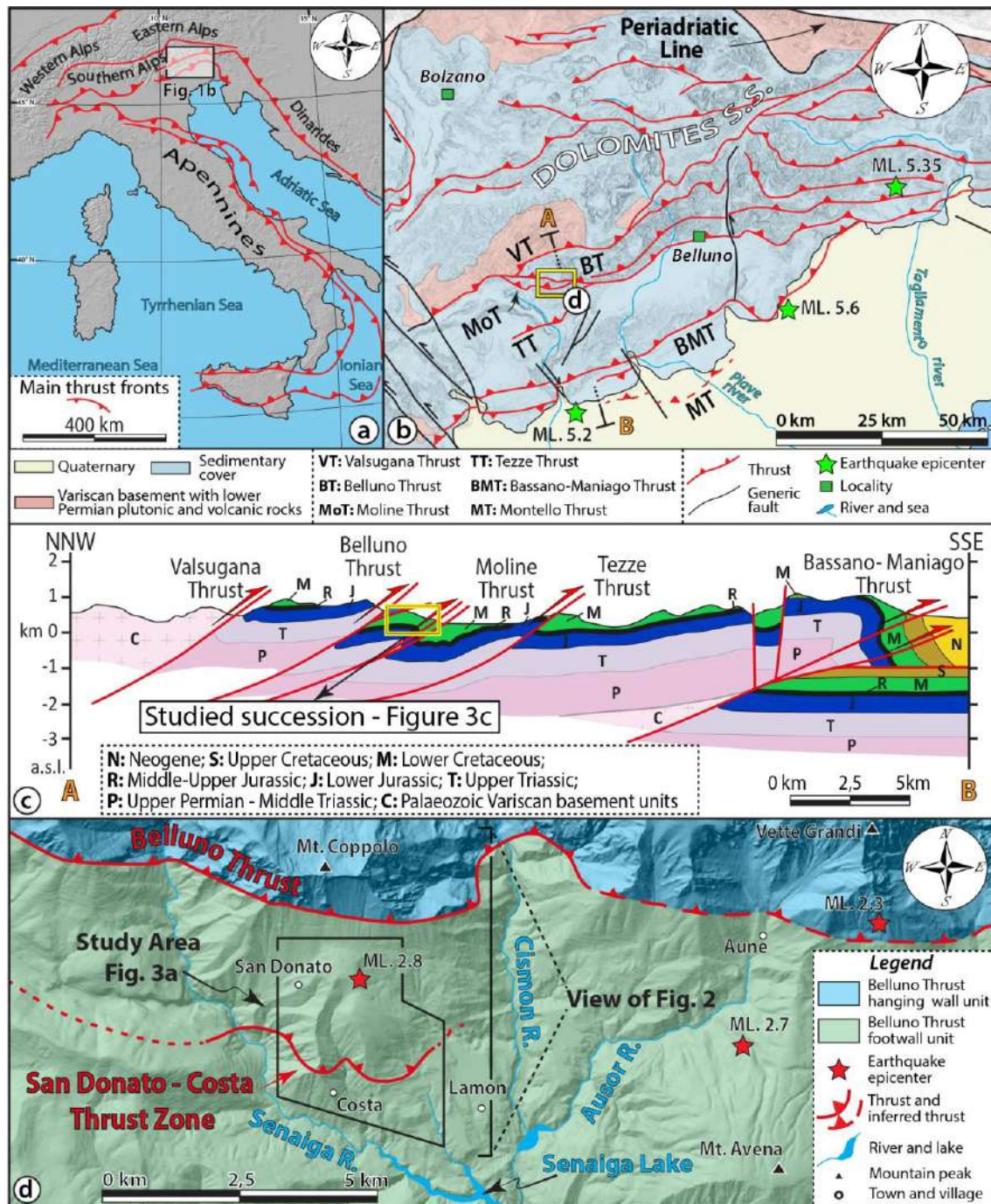


Fig. 1. a) Schematic tectonic framework of Italy showing the main thrust fronts. b) Simplified geological-structural map of the Eastern Southern Alps (ESA) southern sector in the Belluno Thrust (BT) area (redrawn and modified after [Castellarin & Cantelli, 2000](#) and [Doglioni, 1990](#)); shown earthquake epicentres are the three of the most destructive events of the ESA ([Galadini et al., 2005](#)). c) Representative geological cross-section across the ESA (redrawn and modified after [Selli, 1998](#); [Bosellini et al., 2003](#); [Doglioni & Carminati, 2008](#)). The trace of the geological section is shown in (b). d) Simplified geological map of the area encompassing the Belluno Thrust (BT) and the San Donato-Costa Thrust Zone (modified from [Zuccari et al., 2021](#)). The location of the study area is indicated. The epicentres of the three most recent earthquakes ([ISIDE database](#)) affecting the study area since 1985 are reported.

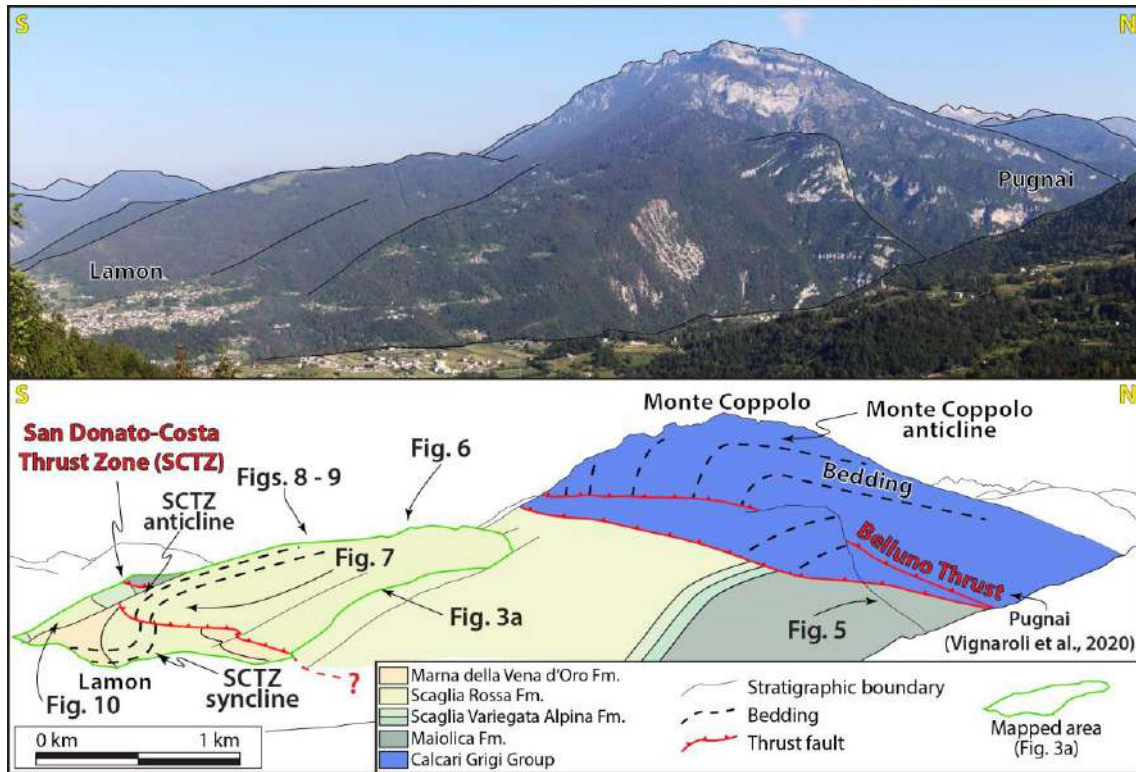


Fig 2. Panoramic view of part of the study area showing the San Donato-Costa Thrust Zone dissecting the footwall succession of the Belluno Thrust. Note the bedding attitude deformed by thrust-related anticlines and synclines.

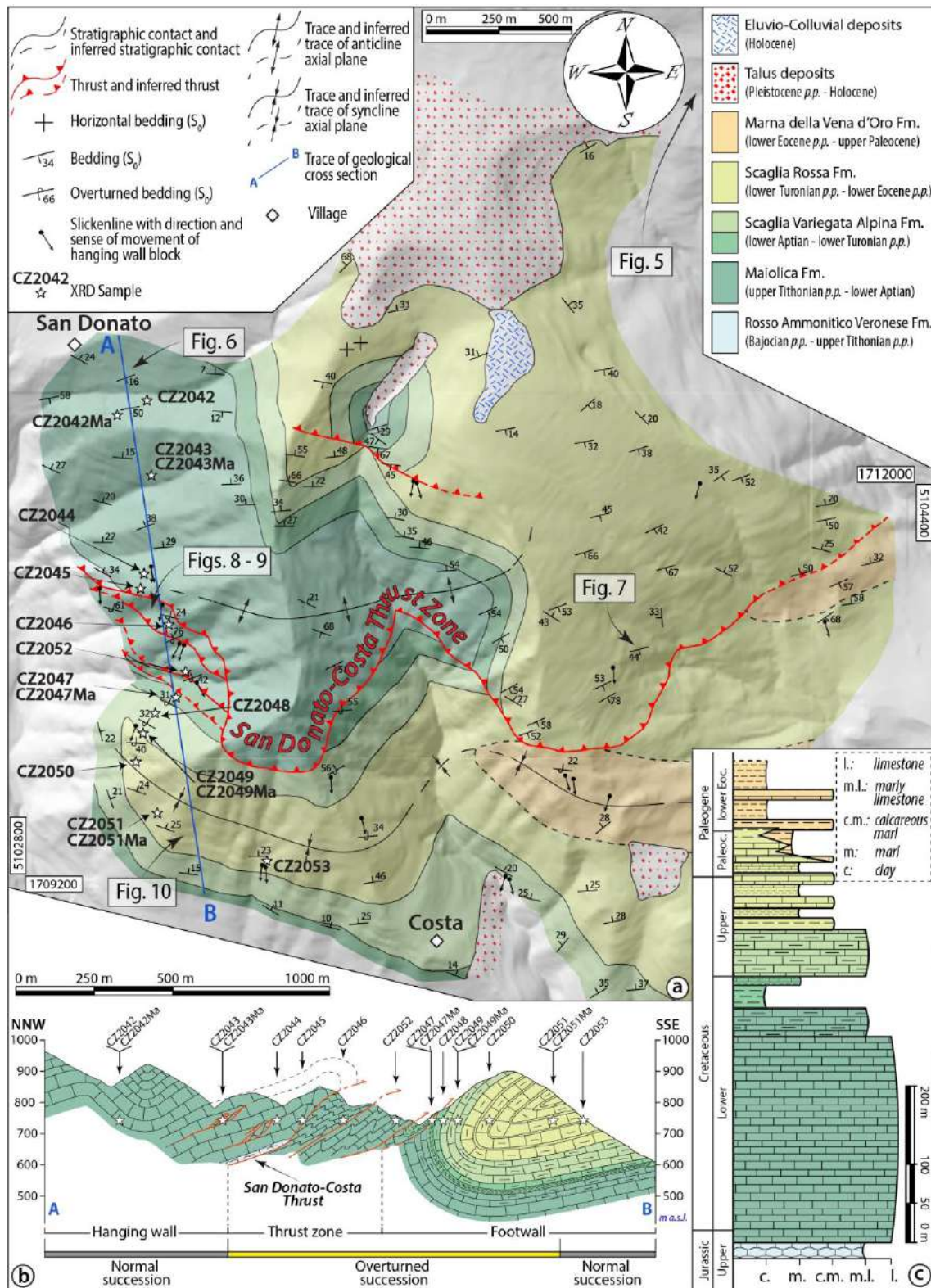


Fig. 3. a) Geological map of the San Donato-Costa Thrust Zone (after Zuccari et al., 2021). b) Representative geological cross-section across the thrust. c) Stratigraphic and lithological column of the sedimentary multilayer succession deformed by the thrust. Locations of XRD samples shown in (a) and (b). l.: limestone; m.l.: marly limestone; c.m.: calcareous marl; m.: marl; c.:clay.

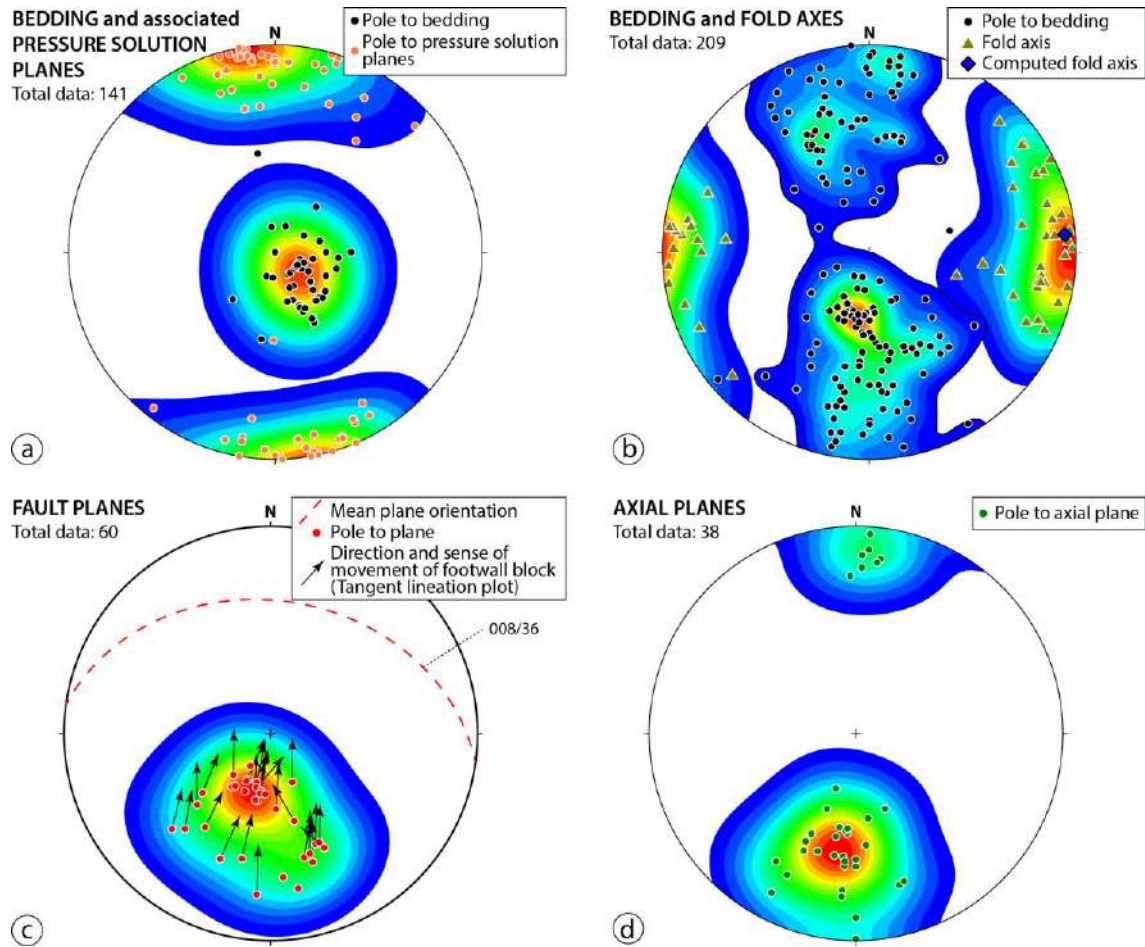


Fig. 4. Lower hemisphere stereographic projections (Schmidt net) of measured structural elements. a) Contours of poles to bedding and poles to pressure solution planes of the northern portion of the hanging wall domain. b) Contour of poles to bedding, fold axes and computed fold axis (“Bingham Analysis” on pole to bedding). c) Contour of poles to fault planes with tangent lineation data displaying the direction and sense of movement of fault footwall blocks. d) Contour of poles to axial planes. Kamb contour values: interval = 1, Significance level = 2 (Kamb, 1959).

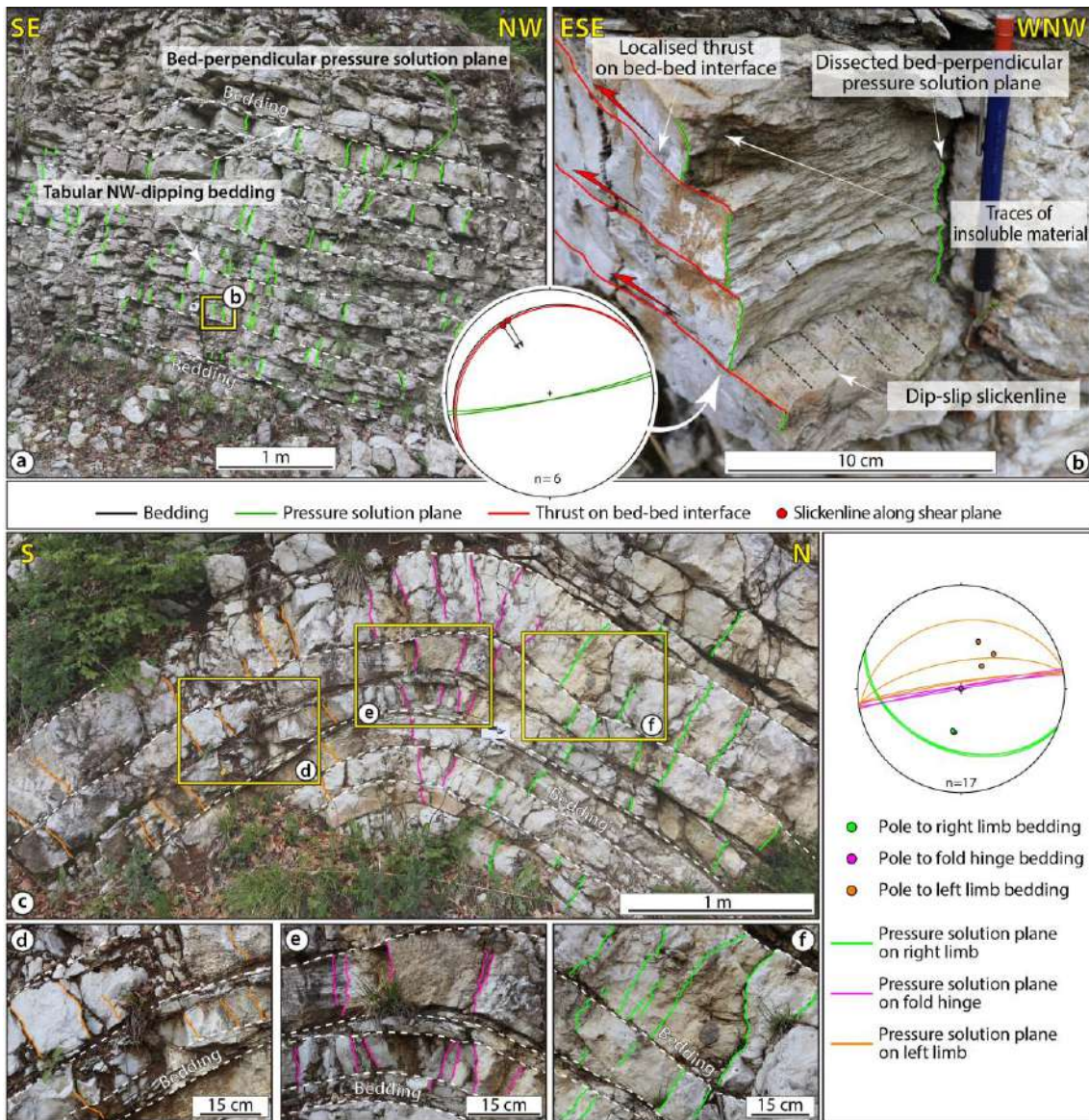


Fig. 5. Pressure-solution planes within the Maiolica Fm. in the northern hanging wall domain of the SCTZ. a) Tabular NW-dipping succession with pervasive bed-perpendicular pressure solution planes. b) Bedding parallel thrust surfaces dissecting the pressure solution planes. c) WNW-trending open buckle fold characterised by pervasive bed-perpendicular pressure-solution planes. d) N-dipping pressure solution planes on S-dipping limb. e) Sub-vertical pressure solution planes in fold hinge. f) S-dipping pressure solution planes on the N-dipping limb. Colours of structural elements in (a) and (f) are consistent with those reported in the Schmidt nets (lower hemisphere projection).

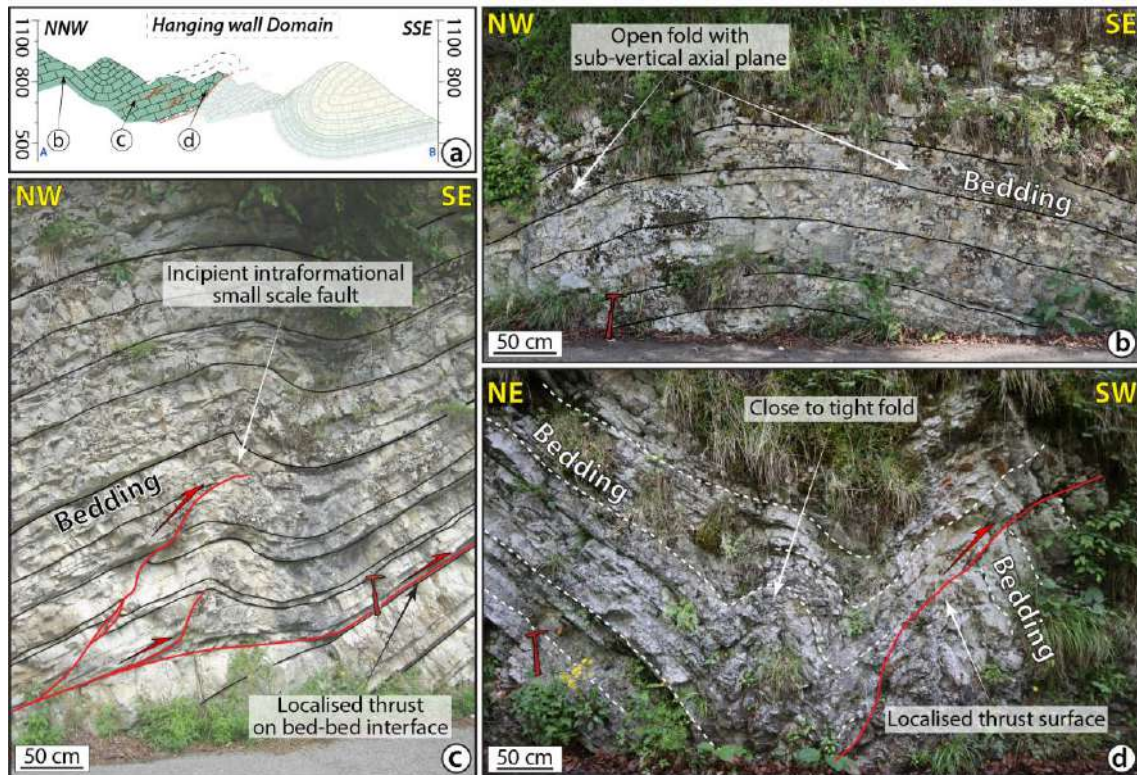


Fig. 6. Deformation structures within the Maiolica limestone in the SCTZ hanging wall domain. a) Location of studied outcrops along the SCTZ section. b) Open upright fold with metric wavelength and amplitude. c) Folds with wavelength of ~ 90 cm and amplitude of ~ 40 cm. Low-displacement top-to-the SE reverse faults cut across the folded sequence. d) Close to tight fold near the SCTZ.

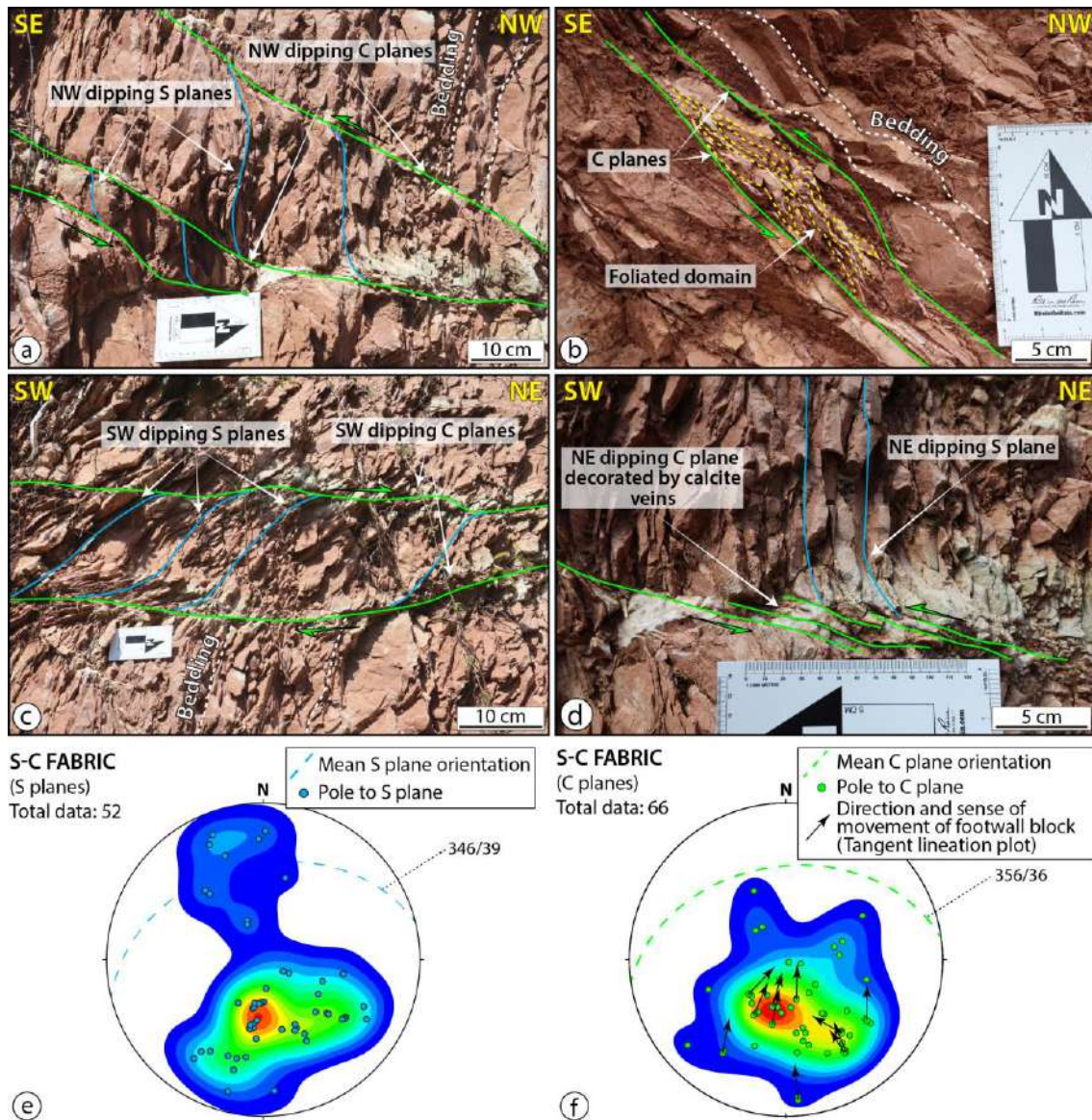


Fig. 7. Deformation structures within the eastern sector of the SCTZ hanging wall domain. a) S-C fabric deforming the sub-vertical forelimb within the more marly portion of the Scaglia Rossa Fm. b) Foliated domain with S-C fabric in marly interlayers parallel to bedding on gently dipping fold back limb within the Scaglia Rossa Fm. c) Top-to-the NE S-C fabric within the calcareous portion of the Scaglia Rossa Fm. d) Detail of C planes decorated by calcite veins bounded by slip surfaces. e) Contours of poles to S planes; mean S plane orientation shown by dashed great circle. f) Contours of poles to C planes; mean C plane orientation shown by dashed green great circle. Lower hemisphere Schmidt net projections. Kamb contour values: interval = 1, Significance level = 2 (Kamb, 1959).



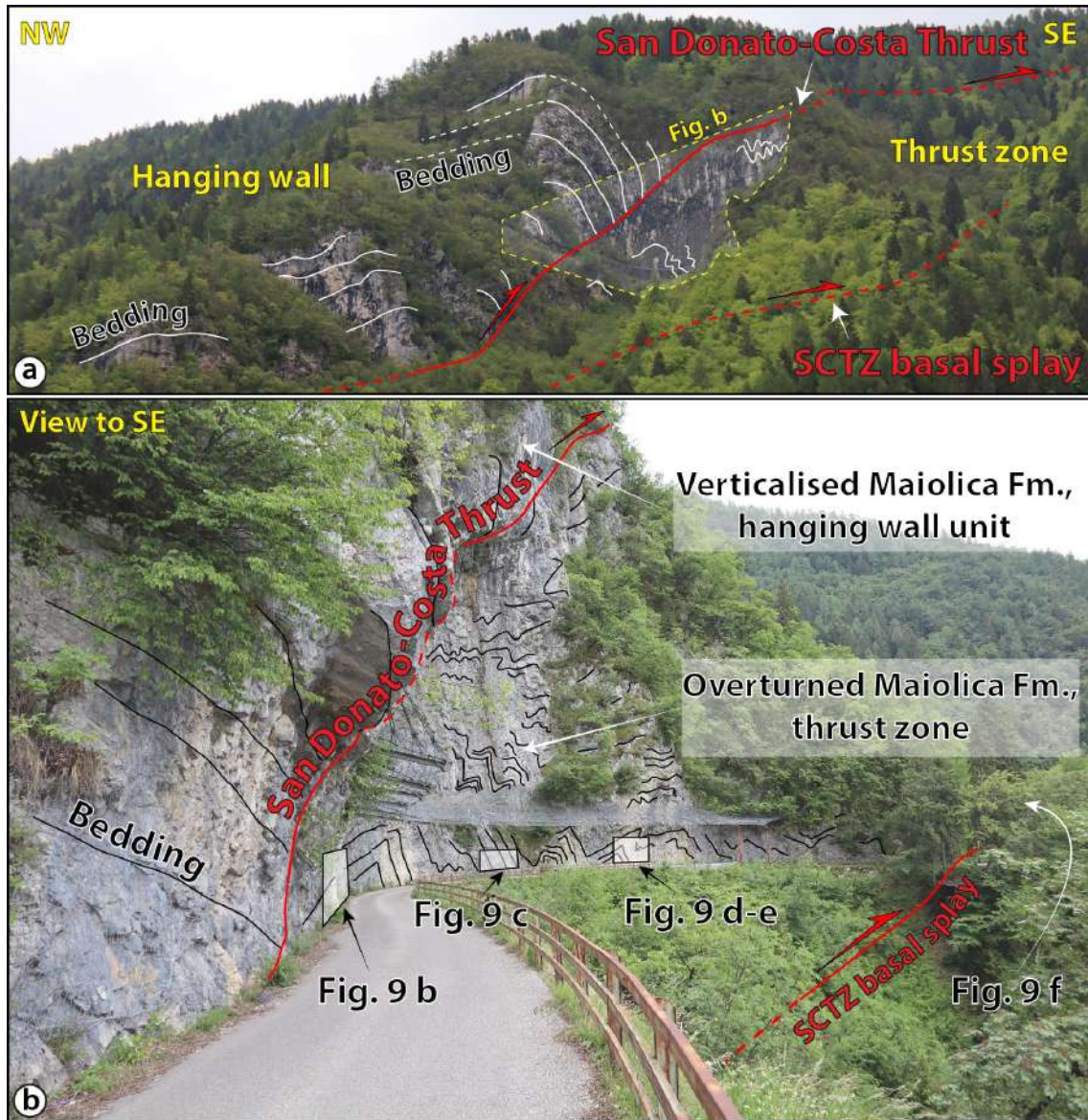


Fig. 8. Panoramic view of the San Donato-Costa Thrust zone (SCTZ). a) Panoramic view of the main hanging wall anticline of the SCTZ. Note the difference in folding style between hanging wall and footwall. b) Detailed view of the SCTZ footwall containing asymmetric and faulted folds within the overturned Maiolica Fm.

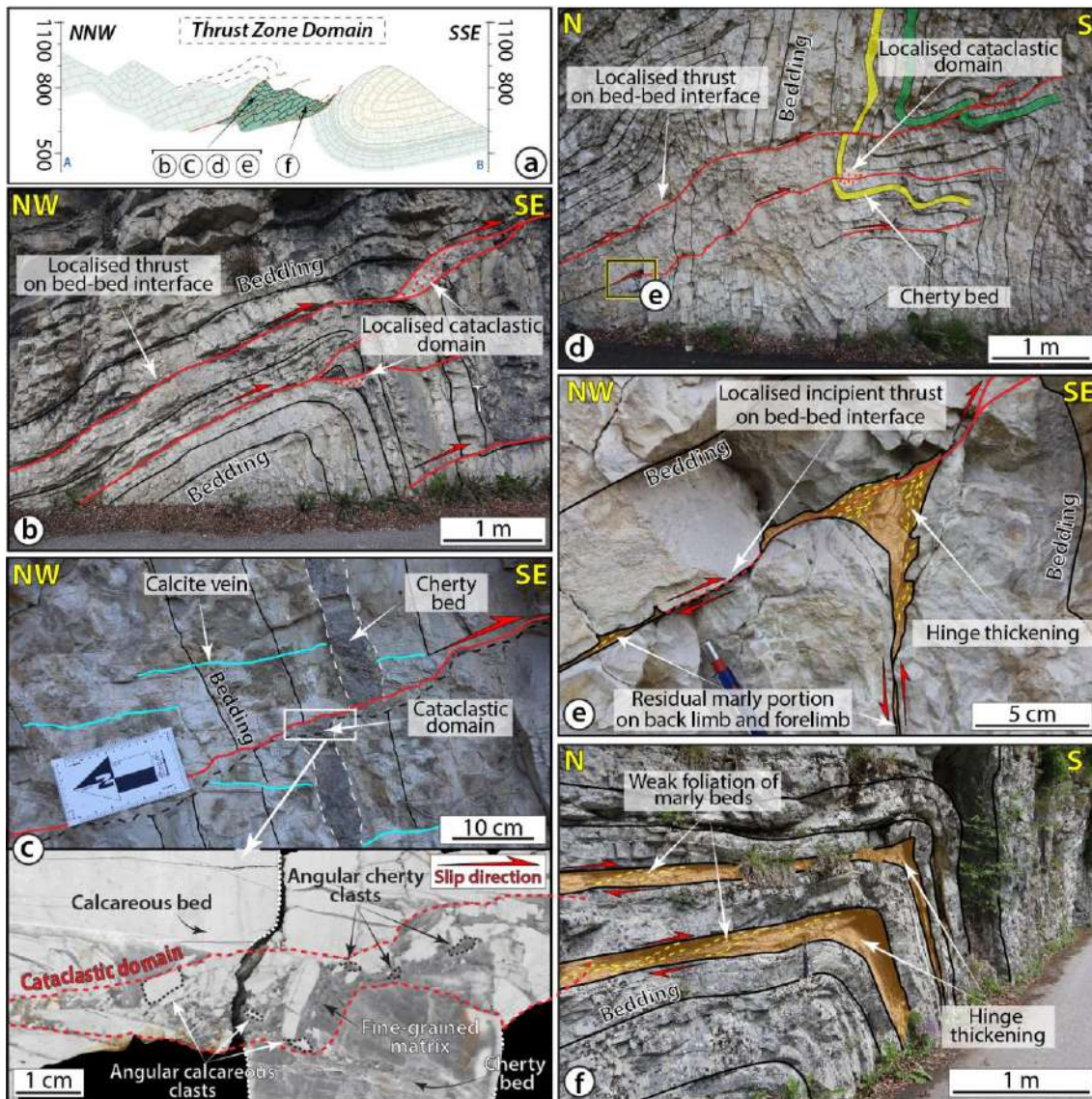


Fig. 9. Deformation structures within the thrust zone domain. a) Location of the studied outcrops. b) Asymmetric and SE-verging fold with multiple reverse faults cutting through the verticalized forelimb (note the associated cataclasite). c) Localised cataclastic domain along the verticalized beds of the Maiolica Fm. (top) and detail of the polished hand specimen of the cataclastic domain, composed of mixed calcareous and cherty clasts (bottom). d) Multiple reverse faults with centimetric offset cutting through the verticalized forelimb of a S-verging anticline. e) Foliated marls in hinge thickened by marl flow during progressive folding. f) Asymmetric and SE-verging fold and marly interbeds deformed in response to flexural slip and layer-parallel shearing (LPS) during progressive folding.

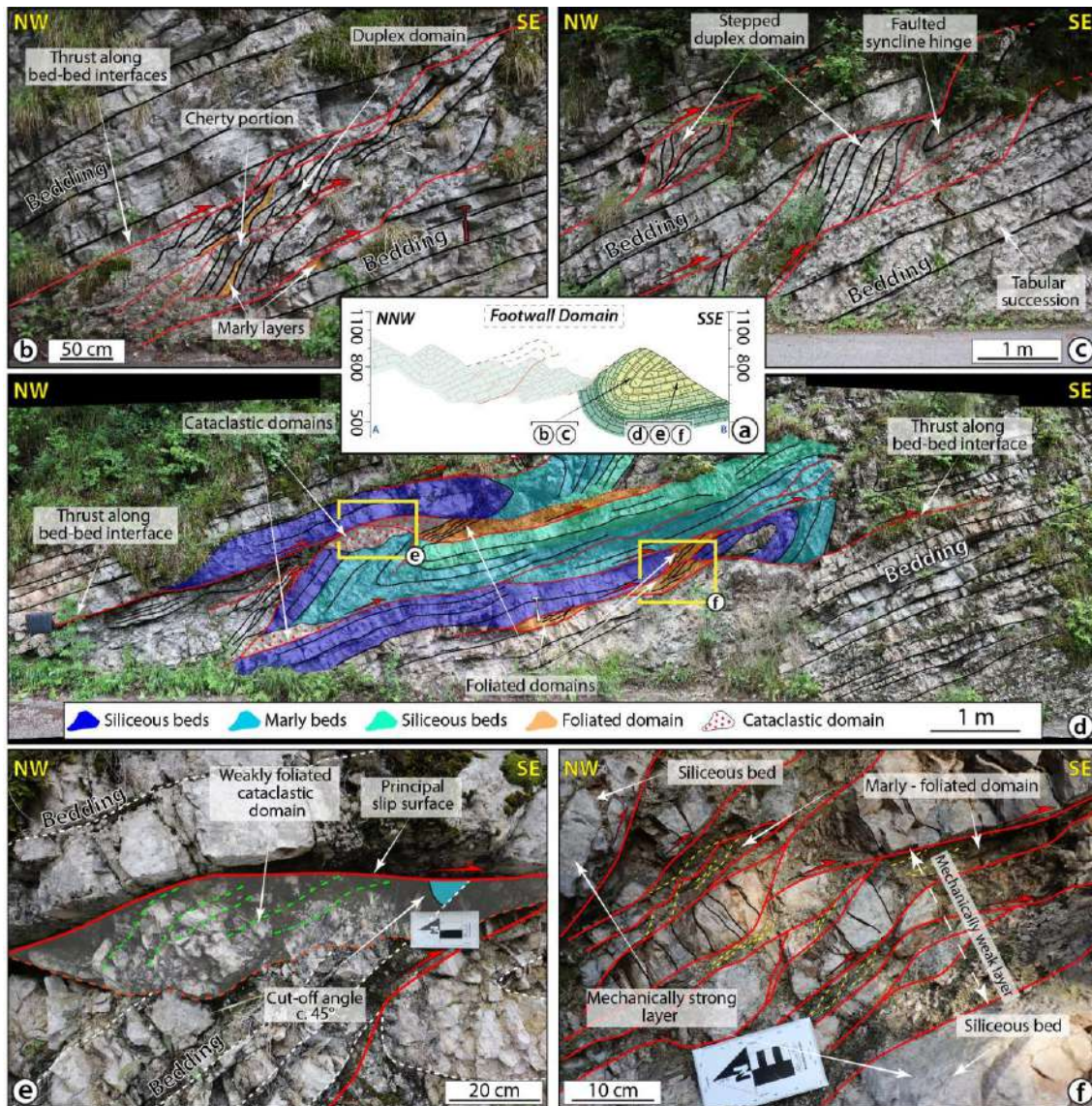
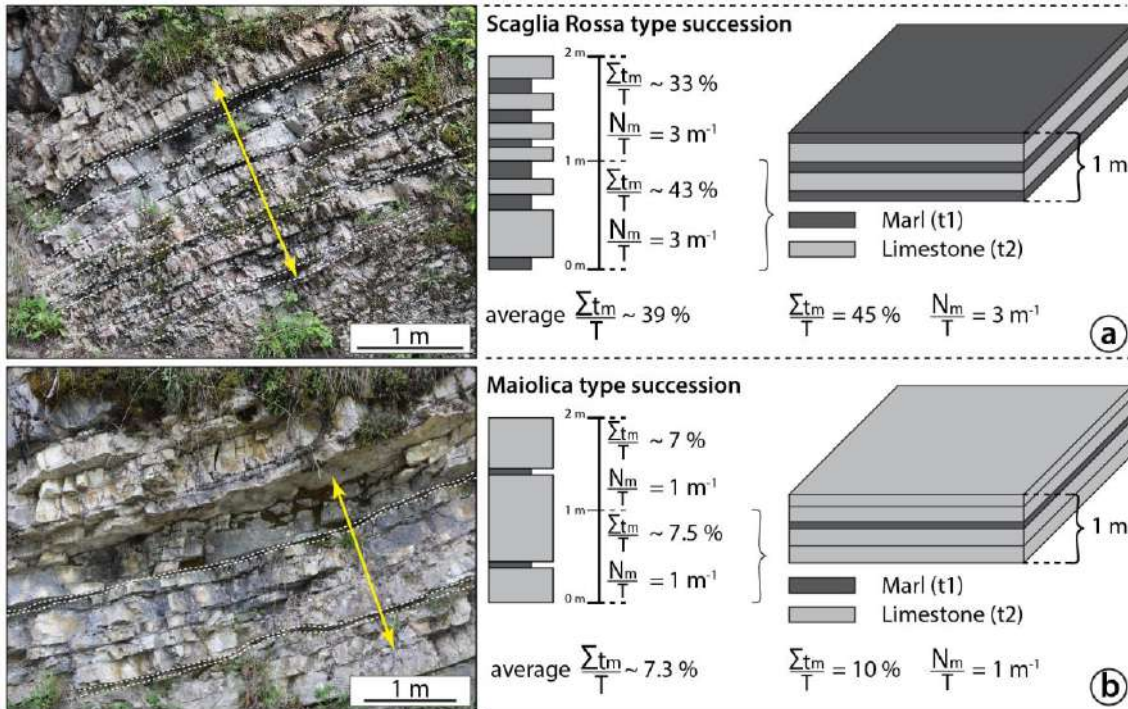


Fig. 10. a) Location of the studied outcrops; b) Marly beds transposed along horses within duplex domain. c) Duplex domain within the steeply dipping syncline back limb. d) m-scale duplex structures defined by N-dipping and top-to-the SE floor and roof thrusts. Centimetric to decimetric asymmetric lithons of siliceous and marly beds embedded within pervasively foliated marly beds. e) Incipient cataclastic domain with oblique foliation concordant with top-to-the S sense of shear. f) Foliated domain with multiple sigmoidal calcareous lithons attesting to top-to-the SE sense of shear.

## Lithotype endmembers



## Fold limb and thrust dip angles

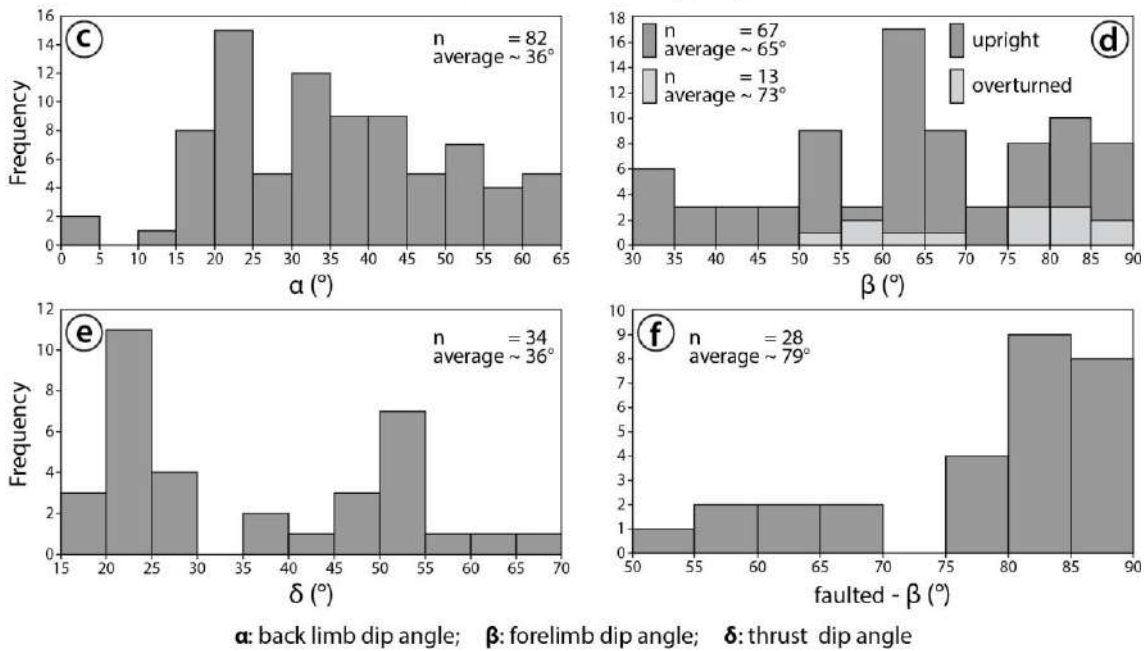


Fig. 11. Definition of the endmember lithotypes and of the geometrical relationships between back limb, forelimb and thrust surface dip angle. a) and b) Field analogue and conceptualisation of the Scaglia Rossa and Maiolica endmembers, respectively, reporting the thickness of marly and calcareous beds with respect to the reference measured succession. c) Readings of back limb dip angles ( $\alpha$ ). d) Readings of forelimb dip angles ( $\beta$ ). e) Reading of thrust fault dip angles ( $\delta$ ). f) Readings of forelimb dip angles of limbs cut by thrust faults. Data are from 82 folds and 34 thrusts from the study area.  $\Sigma t_m/T$ : ratio between the cumulative thickness of marly layers and the total thickness of the measured succession;  $N_m/T$ : ratio between the number of marly layers and the total thickness of the measured succession.

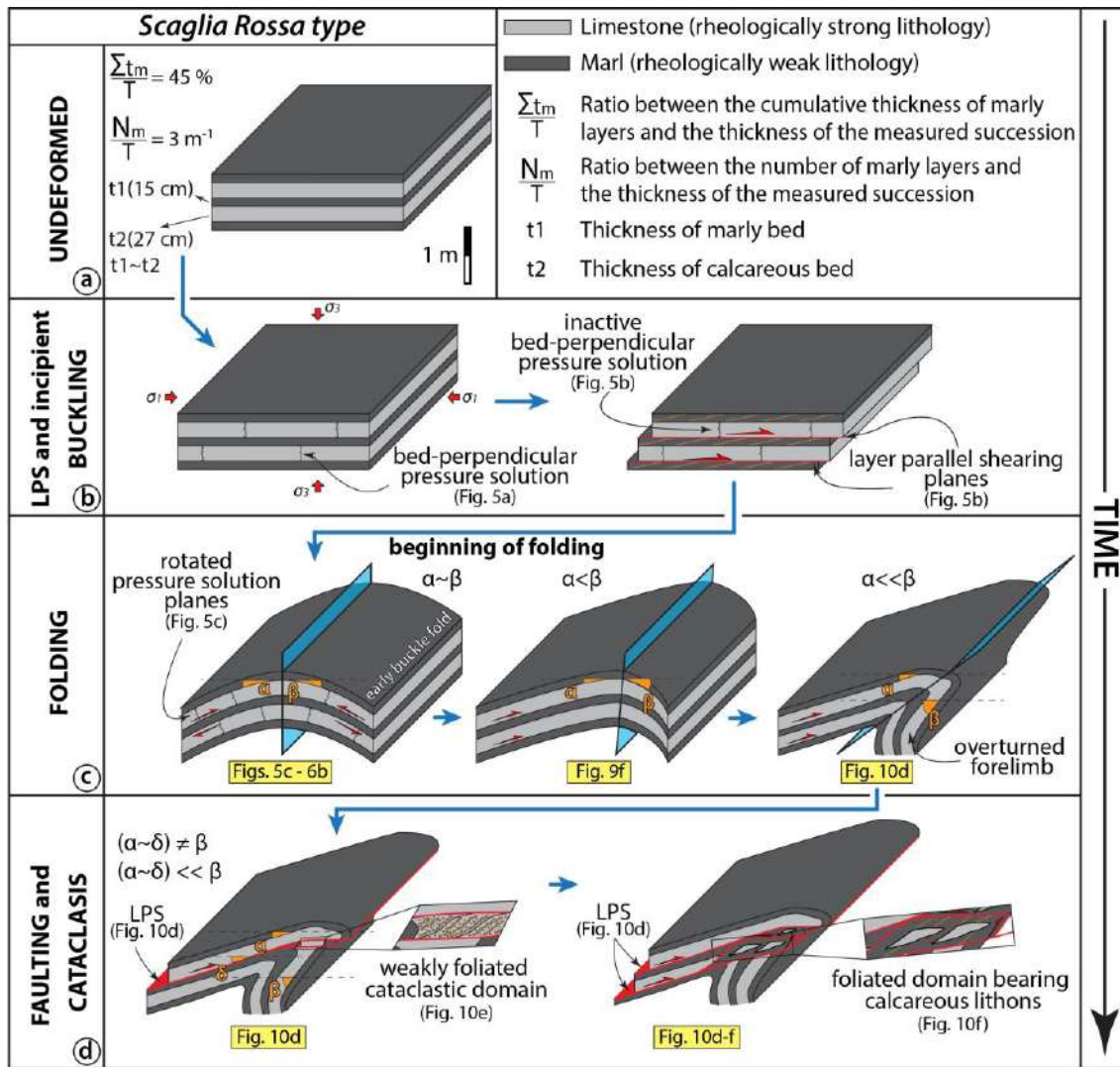


Fig. 12. Deformation model for the Scaglia Rossa endmember. a) The starting condition represents the middle portion of the Scaglia Rossa Fm. in the study area, with  $\frac{\sum t_m}{T} = 45\%$  and  $\frac{N_m}{T} = 3 \text{ m}^{-1}$ . b) Layer parallel shortening, layer parallel shearing and incipient buckling stage, showing the bed-perpendicular pressure solution planes and the transition to the progressive shearing along bed-bed interfaces. c) Folding stage showing the progressive fold evolution from symmetric to asymmetric and verging through the steepening of the forelimb. d) Faulting and cataclasis stage showing the “decapitation” of an asymmetric fold, where the thrust localises along the marly layers, and the progressive evolution and widening of the fault zone. Yellow labels refer to outcrop examples shown in the indicated figure. LPS: Layer Parallel Shearing.

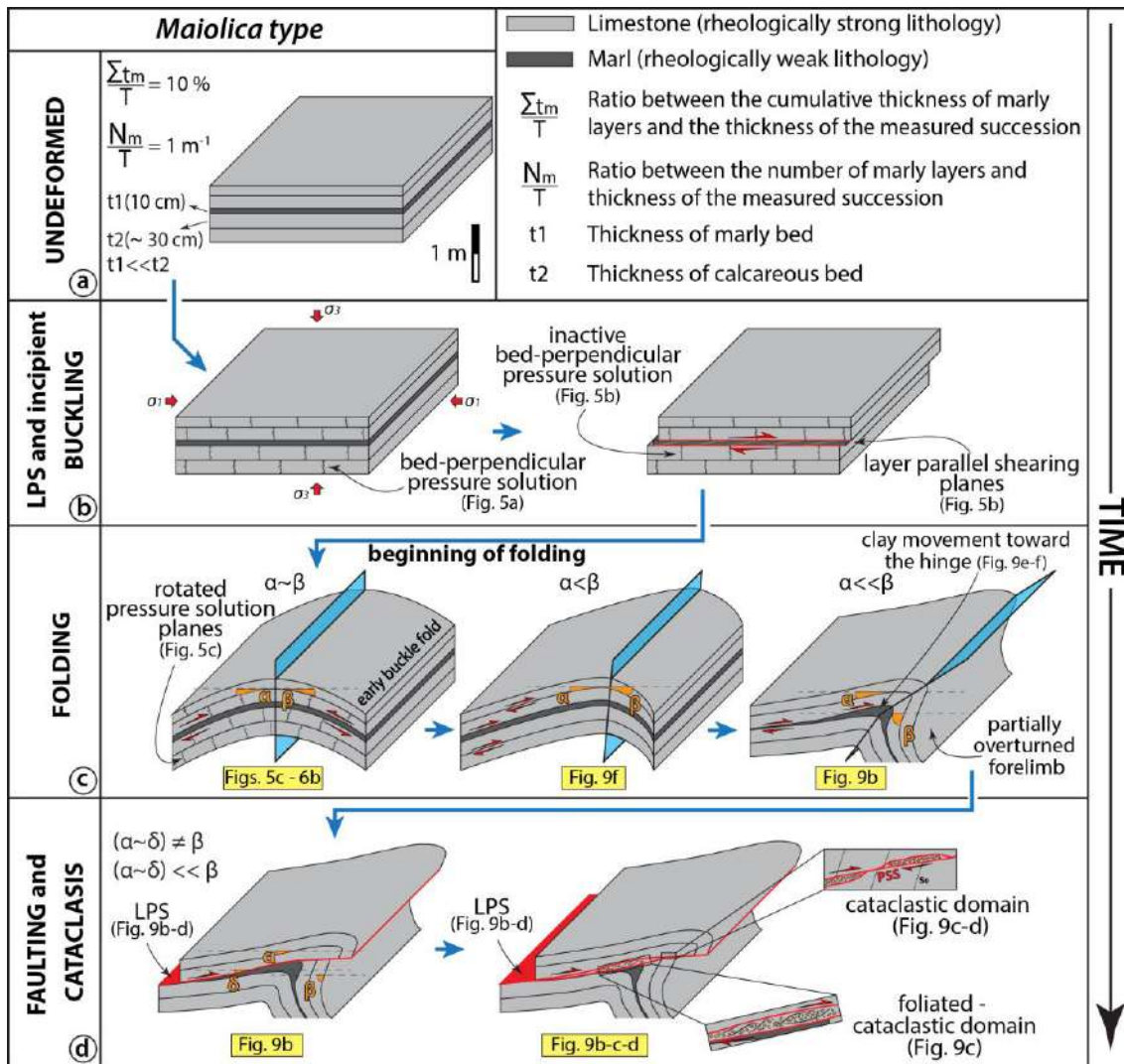


Fig. 13. Deformation model for the Maiolica endmember. a) The starting condition represents the middle and most calcareous portion of the Maiolica Fm. in the study area, with  $\sum t_m/T = 10\%$  and  $N_m/T = 1\text{ m}^{-1}$ . b) Layer parallel shortening, layer parallel shearing and incipient buckling stage, showing the bed-perpendicular pressure solution planes and the progressive evolution into shear along bed-bed interfaces exploiting the only one marly layer. c) Folding stage showing the progressive evolution of fold, starting from the symmetric early buckle fold, with the passive rotation of bed-perpendicular pressure solution planes, from symmetric to asymmetric geometry, related to the continuous steepening of forelimb. d) Faulting and cataclasis stage showing the development of a discrete thrust that localises along one single marly layer and “decapitation” of the asymmetric fold. The second part of this stage shows the evolution and widening of the fault zone by also considering the involved rock type (marly vs. calcareous). Yellow labels refer to outcrop examples shown in the indicated figure. LPS: Layer Parallel Shearing.

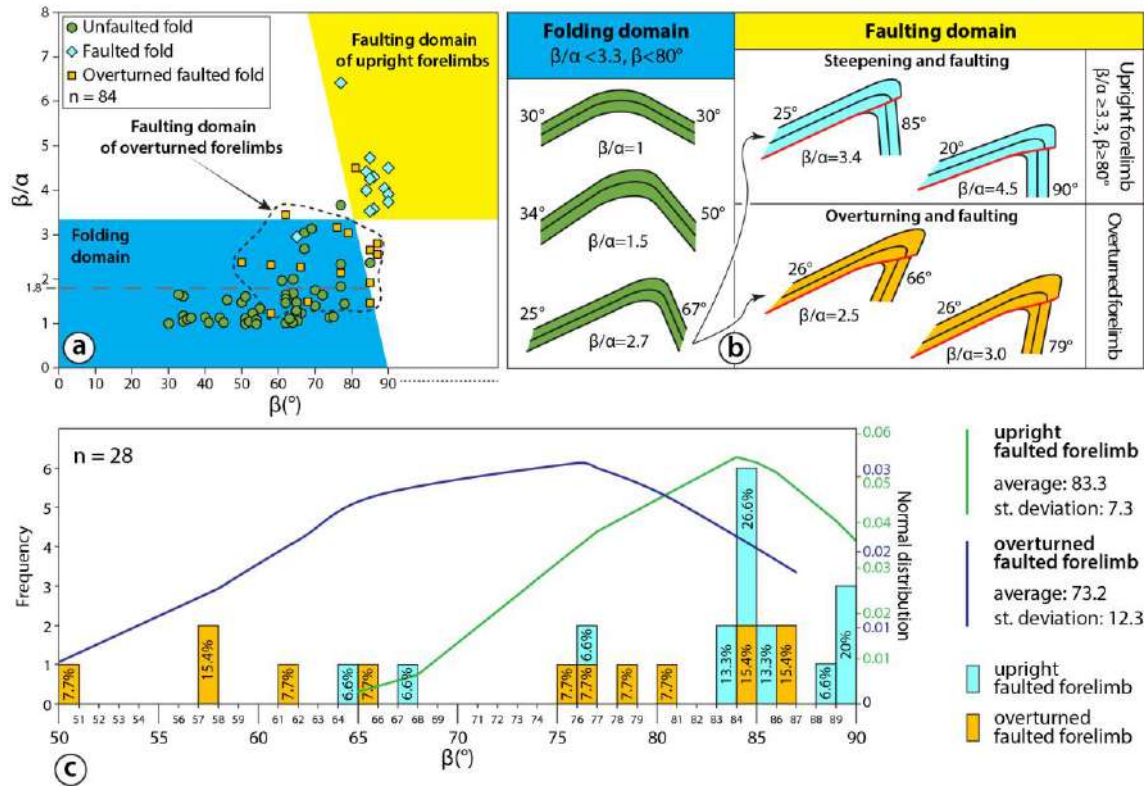


Fig. 14. Quantification of the critical angle from folding to faulting. a) Fields of stability of different deformation mechanisms as a function of the variation of the fold limb dip angle. b) Conceptualisation of back limb and forelimb geometry during folding. c) Frequency of forelimb dip angle of faulted folds and normal data distribution.

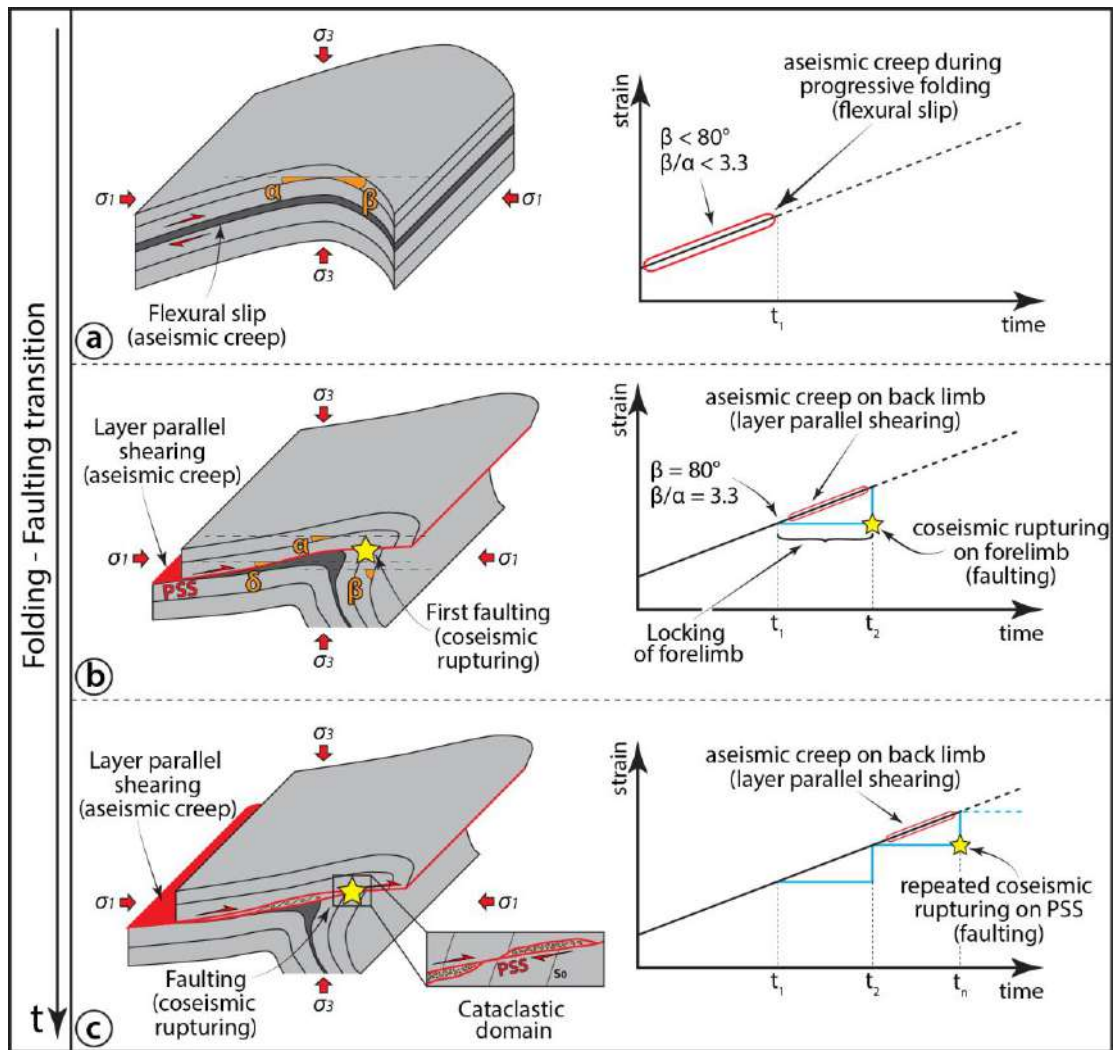


Fig. 15. Conceptual model of strain localisation during the folding-faulting transition and related aseismic vs seismic behaviour. a) Folding stage, where flexural slip develops aseismically along bed-bed interfaces ( $\beta < 80^\circ$  and  $\beta/\alpha < 3.3$ ). b) First stage of faulting after the fold-locking stage ( $t_1$ ,  $\beta = 80^\circ$  and  $\beta/\alpha = 3.3$ ): layer parallel shearing deforms the back limb, exploiting bed-bed interfaces, in an aseismic regime, whereas simultaneous seismic faulting dissects the forelimb ( $t_2$ ) with localised slip and fracturing. c) Evolved faulting ( $t_n$ ) inducing repeated seismic rupturing along newly formed principal slip surfaces (PSS) during widening of the fault zone and development of the cataclastic domain, whereas aseismic deformation of the back limb acts via layer parallel shearing.